Vertical Structure of the Upper–Indian Ocean Thermal Variability

YUANLONG LI

Key Laboratory of Ocean Circulation and Waves, Institute of Oceanology, Chinese Academy of Sciences, and Function Laboratory for Ocean Dynamics and Climate, Qingdao National Laboratory for Marine Science and Technology, and Center for Ocean Mega-Science, Chinese Academy of Sciences, Qingdao, and CAS Center for Excellence in Quaternary Science and Global Change, Xi'an, China

WEIQING HAN

Department of Atmospheric and Oceanic Sciences, University of Colorado Boulder, Boulder, Colorado

FAN WANG

Key Laboratory of Ocean Circulation and Waves, Institute of Oceanology, Chinese Academy of Sciences, and Function Laboratory for Ocean Dynamics and Climate, Qingdao National Laboratory for Marine Science and Technology, and Center for Ocean Mega-Science, Chinese Academy of Sciences, Qingdao, China

LEI ZHANG

Department of Atmospheric and Oceanic Sciences, University of Colorado Boulder, Boulder, Colorado

JING DUAN

Key Laboratory of Ocean Circulation and Waves, Institute of Oceanology, Chinese Academy of Sciences, and Function Laboratory for Ocean Dynamics and Climate, Qingdao National Laboratory for Marine Science and Technology, and Center for Ocean Mega-Science, Chinese Academy of Sciences, Qingdao, China

(Manuscript received 17 November 2019, in final form 5 June 2020)

ABSTRACT

Multi-time-scale variabilities of the Indian Ocean (IO) temperature over 0–700 m are revisited from the perspective of vertical structure. Analysis of historical data for 1955–2018 identifies two dominant types of vertical structures that account for respectively 70.5% and 21.2% of the total variance on interannual-to-interdecadal time scales with the linear trend and seasonal cycle removed. The leading type manifests as vertically coherent warming/cooling with the maximal amplitude at ~100 m and exhibits evident interdecadal variations. The second type shows a vertical dipole structure between the surface (0–60 m) and subsurface (60–400 m) layers and interannual-to-decadal fluctuations. Ocean model experiments were performed to gain insights into underlying processes. The vertically coherent, basinwide warming/cooling of the IO on an interdecadal time scale is caused by changes of the Indonesian Throughflow (ITF) controlled by Pacific climate and anomalous surface heat fluxes partly originating from external forcing. Enhanced changes in the subtropical southern IO arise from positive air–sea feedback among sea surface temperature, winds, turbulent heat flux, cloud cover, and shortwave radiation. Regarding dipole-type variability, the basinwide surface warming is induced by surface heat flux forcing, and the subsurface cooling occurs only in the eastern IO. The cooling in the southeast IO is generated by the weakened ITF, whereas that in the northeast IO is caused by equatorial easterly winds through upwelling oceanic waves. Both El Niño–Southern Oscillation (ENSO) and IO dipole (IOD) events are favorable for the generation of such vertical dipole anomalies.

Supplemental information related to this paper is available at the Journals Online website: https://doi.org/10.1175/JCLI-D-19-0851.s1.

Corresponding author: Yuanlong Li, liyuanlong@qdio.ac.cn

DOI: 10.1175/JCLI-D-19-0851.1

1. Introduction

Historical ocean observations since the mid-twentieth century documented prominent thermal variations in the upper Indian Ocean (IO) on time scales ranging from interannual to interdecadal. Research efforts have been devoted to understanding these variabilities and their relationships with global and regional climate variability and change (e.g., Xie et al. 2002, 2009; Schott et al. 2009; Han et al. 2014a; and references therein). Thermal variabilities of the upper IO are actively involved in many of the most influential climate phenomena such as the Asian–African–Australian monsoons and El Niño–Southern Oscillation (ENSO) (e.g., Gadgil et al. 1984; Latif et al. 1999; Webster et al. 1999; Schott and McCreary 2001; Xie et al. 2002; Annamalai et al. 2005, 2007) and exert strong influence on behaviors of tropical cyclones, intraseasonal oscillations, and synoptic marine heatwaves (e.g., Maloney and Sobel 2004; Neetu et al. 2012; Pearce and Feng 2013; Feng et al. 2015; Ramsay et al. 2017), with socioeconomic impacts felt in the surrounding populated landmasses. Recently, the community has realized the vital role of IO in modulating the global surface warming rate. Subsurface heat storage of the IO significantly contributed to the decelerated global surface warming rate during the early twenty-first century (e.g., England et al. 2014; Lee et al. 2015; Nieves et al. 2015; Li et al. 2017). Understanding and prediction of the upper-IO thermal variabilities on various time scales have been the central theme for the IO research. The mechanisms controlling interannual, decadal, and interdecadal variabilities show dramatic differences, and our understanding of the underlying dynamics remains far from complete, as elaborated below.

ENSO and the IO dipole mode (IOD) are the primary sources of interannual variability of the tropical IO. The El Niño condition in the Pacific facilitates the occurrence of a positive IOD in boreal fall (Annamalai et al. 2003) and tends to cause a basinwide sea surface temperature (SST) warming over the tropical IO prolonged from winter through next year's summer (e.g., Chambers et al. 1999; Klein et al. 1999; Huang and Shukla 2007a; Du et al. 2009). A positive IOD is characterized by cooling near Sumatra–Java coasts and prevailing warming of the western tropical IO (Saji et al. 1999). Some IOD events can operate independently from ENSO and modulate the ENSO cycle (Behera and Yamagata 2001; Izumo et al. 2010; Yuan et al. 2011; Duan et al. 2020). In comparison with SST, our knowledge of subsurface variability is much more fragmental (e.g., Huang and Shukla 2007b; Trenary and Han 2012; Sayantani and Gnanaseelan 2015; Deepa et al. 2018). Anomalous easterly winds near the equator during positive IOD events cause subsurface cooling in the eastern equatorial IO that subsequently spreads to the Bay of Bengal (e.g., Clarke and Liu 1994; Han and Webster 2002; Rao et al. 2002; Rao and Behera 2005) and Sumatra–Java coasts (e.g., Murtugudde et al. 2000; Du et al. 2008; Chen et al. 2016) as coastally trapped waves. ENSO acts as a remote forcing agent for the IO through both an atmospheric bridge and an oceanic channel. Through the atmosphere, surface wind anomalies in the tropical IO generated by El Niño events induce thermocline deepening (subsurface warming) in the southwest tropical IO (e.g., Masumoto and Meyers 1998; Xie et al. 2002; Huang and Kinter 2002; Rao and Behera 2005; Yang et al. 2019). Through the ocean, the variability of Indonesian Throughflow (ITF) associated with ENSO is rather influential for the southern IO. The ITF strengthens under La Niña condition and leads to thermocline depression and upper-ocean warming (e.g., Potemra and Lukas 1999; Wijffels and Meyers 2004; Cai et al. 2005).

Understanding the IO variabilities on decadal-to-multidecadal time scales represent a substantial challenge, due to the short record of in situ and satellite observations. The image emerging from existing studies suggest several processes with competing importance, including anthropogenic forcing from greenhouse gases and aerosols (Cai et al. 2006, 2007; Du and Xie 2008; Dong and Zhou 2014), radiative forcing by volcanic eruptions (Gleckler et al. 2006; Smith et al. 2016), and natural climate variability (for reviews, see Han et al. 2014a, 2018). Decadal and interdecadal climate variability modes of Pacific and Atlantic Oceans have been shown to exert strong influence on the IO (e.g., Lee and McPhaden 2008; Han et al. 2017; X. Li et al. 2016; Xue et al. 2018; Cai et al. 2019). The interdecadal Pacific oscillation (IPO; Power et al. 1999) is the most influential remote forcing (e.g., Han et al. 2018; Deepa et al. 2019; Mohapatra et al. 2020). Similar to the ENSO impacts, the IPO affects the IO through both the ITF (Schwarzkopf and Böning 2011; Trenary and Han 2013; Feng et al. 2004, 2010, 2013, 2015; Li et al. 2017, 2018; Ummenhofer et al. 2017; Jin et al. 2018) and atmospheric teleconnection (e.g., Lee and McPhaden 2008; Han et al. 2017; Zhou et al. 2017; Deepa et al. 2018). Decadal variability in the subtropical south IO is also influenced by ocean internal instabilities, particularly in eddy-rich regions (e.g., Trenary and Han 2013; Li and Han 2015; Sérazin et al. 2016). Recent researches have revealed that the mechanisms for the decadal and

multidecadal variabilities of the IO are likely time varying. The basin-mean SST of the tropical IO used to be roughly in phase with the IPO showing warming under positive IPO condition (Deser and Phillips 2006; Dong et al. 2016) before the 1970s, yet since then it exhibited persistent warming trend and decadal fluctuations out of phase with IPO (Han et al. 2014b). The external forcing effect by greenhouse gases and aerosols has been proposed to explain this relation change (Dong and McPhaden 2017; Zhang et al. 2018a) and supported by increasing evidences from recent studies of surface winds, sea level, and ocean heat content (OHC) (e.g., Takahashi and Watanabe 2016; Thompson et al. 2016; Srinivasu et al. 2017; Li et al. 2017, 2018).

Most studies reviewed above focused on two-dimensional fields, such as SST, sea level, and OHC. The vertical structure of the IO temperature variability is less appreciated. Several studies analyzed historical data and revealed a complicated vertical structure of the upper-IO temperature since the 1960s, with its linear trend showing surface warming accompanied by thermocline cooling (Barnett et al. 2005; Alory et al. 2007; Han et al. 2006). This structure has been attributed primarily to forcing by surface winds over the IO (Han et al. 2006; Trenary and Han 2008), which in part might be associated with anthropogenic warming (Barnett et al. 2005); the reduction of the ITF transport, however, might, also have contributed to the thermocline cooling, as shown in some ocean general circulation model (OGCM) experiments (Schwarzkopf and Böning 2011; Ummenhofer et al. 2017).

Vertical structure of IO thermal variability is critical for understanding IO heat uptake and heat redistribution across the world's oceans, which exhibit prominent interdecadal variability (e.g., Nieves et al. 2015; Cheng et al. 2015, 2018; Lee et al. 2015; Liu et al. 2016; Li et al. 2017, 2018). This paper attempts to understand thermal variabilities in the upper 700 m of the IO from the perspective of vertical structure. As we shall see below, two types of variability stand out and explain the majority (>90%) of observed variance on interannual-to-decadal time scales. Generation mechanisms of the two types of variability are explored using OGCM experiments. We aim to synthesize the existing views of multi-time-scale IO thermal variabilities and add new knowledge to support the understanding and prediction of ocean heat uptake and climate change.

The rest of the paper is organized as follows. Section1 describes the data and model utilized in this study. Section 3 outlines characteristics of the two types of variability identified in the observed and simulated IO thermal variabilities. Section 4 explores dynamical processes modulating the two modes. Finally, section 5 summarizes the main findings of this study and provides necessary discussions.

2. Data and model

a. Datasets and definitions

Three gridded ocean temperature data are utilized to quantify the upper-IO temperature variabilities: 1) the *World Ocean Atlas* (*WOA*) data (Levitus et al. 2009) provided by the National Oceanic and Atmospheric Administration's (NOAA) National Centers for Environmental Information of the United States; 2) the Institute of Atmospheric Physics (IAP) ocean temperature analysis (Cheng et al. 2016, 2017) provided by IAP, Chinese Academy of Sciences; and 3) version 4.2.1 of the Met Office Hadley Centre "EN" series of datasets (EN4.2.1) data (Good et al. 2013) provided by the Met Office of the United Kingdom. All the three datasets provide 1° × 1°, standard-level temperature data of 0–700 m from 1955 through 2018, among which the data of *WOA* are provided in seasonal (3 month) resolution, whereas those of IAP and EN4 are monthly. We resampled IAP and EN4 into 3-month resolution to match *WOA*. The average of *WOA*, IAP, and EN4 is taken as the "observational ensemble mean." In this study, the IO is defined within the Australia–Asia–Africa coastline, north of 40°S, and west of 130°E. The OHC is computed by integrating ocean temperature over the IO within a specific depth range z_1 to z_2,

$$\mathrm{OHC} = \int_{z_2}^{z_1} \rho C_p T \, dz, \tag{1}$$

where T is ocean temperature and ρ and c_p are density and thermal capacity of seawater, respectively.

We use the 1° × 1° Hadley Centre Sea Ice and Sea Surface Temperature (HadISST) data (Rayner et al. 2003) of 1955–2018 to evaluate SST variability. HadISST data are also used to compute the indices of major natural climate modes, including Niño-3.4, dipole mode index (DMI), and IPO index using conventional definitions. The IPO index is computed with the method of Henley et al. (2015), as the SST anomaly difference between the equatorial Pacific (10°S–10°N, 170°E−90°W) and the northwest plus southwest Pacific regions (25°–45°N, 140°E−145°W plus 50°–15°S, 150°E−160°W). Meteorological data of 10-m winds, surface heat fluxes, 2-m air temperature, and total cloud cover are taken from the 1° European Centre for Medium-Range Weather Forecasts (ECMWF) twentieth-century reanalysis (ERA-20C) from 1955 through 2010 (Poli et al. 2016). For all the ocean and atmospheric data mentioned

above, the climatologic seasonal cycle of 1980–2010 and the linear trend of 1955–2010 are removed to obtain the anomaly, and then a five-season low-pass Hanning-window digital filter is applied. The removed linear trend represents multidecadal changes during the past half century under a changing climate, particularly the responses to anthropogenic greenhouse gas forcing. We are also aware that the heating effect by greenhouse gases is not linear, and an acceleration of warming remains in the later part of the detrended data and contributes to the interdecadal variability of the IO temperature.

b. *HYCOM and experiments*

The Hybrid Coordinate Ocean Model (HYCOM), version 2.2.18 (Bleck 2002), is implemented to the region of Indo-Pacific Oceans between 55°S and 50°N and 19°E and 68°W . The model resolution is $^1/_3° \times ^1/_3°$ in the tropical west Pacific–east IO region (25°S–25°N; 70°–170°E) and gradually changes to 1° × 1° in the midlatitudes (poleward of 44°), eastern Pacific (east of 160°W), and western IO (west of 40°E) [see Fig. S1 of Li et al. (2017)]. The model has 35 hybrid layers with a top layer thickness of 5 m. On the northern and southern open-ocean boundaries, 5° sponge layers are applied, where the model temperature and salinity are relaxed to monthly climatology. Surface forcing fields, including 10-m wind speed, surface wind stress, surface net shortwave and longwave radiations (SWR and LWR), precipitation, and 2-m air temperature and humidity, are all taken from ERA-20C data. Monthly climatologic discharge data of Dai et al. (2009) are used to represent river freshwater input. Wind stress and wind speed are separately exerted onto the model ocean, which can affect the ocean through different processes. Wind stress drives ocean dynamical processes such as advection, upwelling/downwelling, and turbulent mixing, whereas wind speed determines surface turbulent heat flux (latent plus sensible heat fluxes) and evaporation. Turbulent heat fluxes and evaporation rate are computed in an online manner using bulk formula.

The spinup run integrated for 30 years until reaching a quasi-equilibrium stage. Subsequently, the model was integrated forward from 1940 to 2010 under daily surface forcing of ERA-20C fields. This run is named ''main run'' (MR) and used as the reference solution. Our recent studies performed extensive comparisons between MR and various sources of observational data and showed that MR could reproduce with fidelity the mean state and interannual-to-interdecadal variabilities of SST, sea level, and OHC of the IO (Li et al. 2017, 2018, 2019; Zhang et al. 2019). Two additional experiments were performed. To evaluate the effect of Pacific climate through the ITF heat transport, the ''Pacific run'' (PAC) uses daily forcing in the Pacific Ocean (identical to MR), but monthly climatologic forcing in the IO [see Fig. S1 of Li et al. (2017)]. The difference between MR and PAC, that is, MR–PAC, can roughly represent the local atmospheric forcing effect within the IO. The third experiment is the ''wind stress run'' (TAU), which adopts daily wind stress as in MR and monthly climatology for other forcing fields. TAU can represent the effect of wind stress-driven ocean dynamical processes, whereas MR–TAU can be used to evaluate the effect of surface heat fluxes on the IO temperature. Results of these HYCOM runs are processed in the same manner as observational data.

3. Two dominant types of thermal variability

Time evolutions of the observed temperature averaged over the IO basin (Figs. 1a–c) exhibited pronounced variations with typical warming/cooling amplitudes of 0.1–0.3 K. Interannual anomalies, such as the warmings occurred in 1997–98, 2009–10, and 2015–16, are most prominent in the surface layer (0–60 m) and superimposed on lower-frequency anomalies that occupied the entire upper 400 m, such as the warming of 1977–90, the cooling of 1991–2002, and the subsequent warming. Out-of-phase anomalies between the surface and subsurface layers were obvious in 1969–70, 1971, 1974, 1984–85, 1989–90, 1998, and 2007. Such vertical ''dipole'' structures were frequently observed before ~1990 and afterward overwhelmed by recent enhancement of the vertically coherent anomalies. The simulated variations by HYCOM MR are shown in Fig. 1d for comparison. The observed variability characteristics are faithfully reproduced since the late 1970s. Evident discrepancies were detected prior to that time. In 1955–65, the observed IO displayed a subsurface warming, but HYCOM showed a cooling. HYCOM also showed persistent subsurface warming in the 1970s, which was not evident in observation. Satellite observational data were available since the late 1970s, before which atmospheric reanalysis products show apparent discrepancies over the IO (e.g., Han et al. 2010, 2017; Li et al. 2018). These observation-based datasets are also questionable, given the inadequate sampling in the IO and discrepancies among *WOA*, IAP, and EN4 (e.g., Wang et al. 2018; Cheng et al. 2018).

Vertically coherent anomalies on decadal-to-interdecadal time scales are more evident in HYCOM than in observation, possibly owing the superimposition of strong interannual fluctuations. We checked the 6-yr low-pass-filtered anomaly fields (Fig. S1a in the online supplemental material) and confirmed the existence of such variations broadly consistent with HYCOM results (Fig. S1d). The simulated

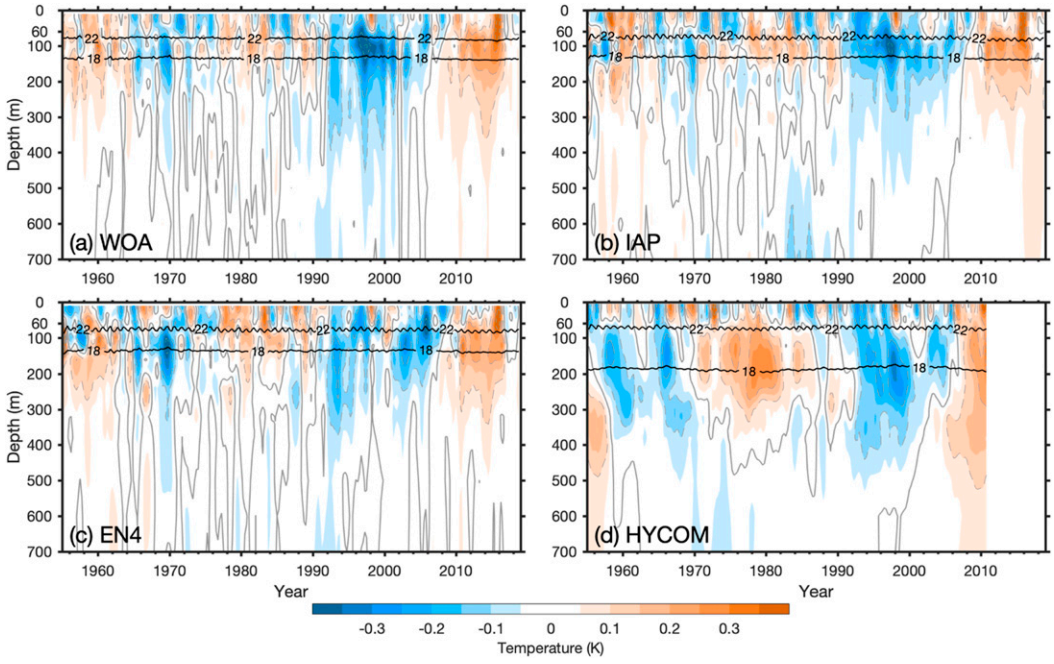

FIG. 1. Evolution of IO basin-mean temperature in the upper 700 m from (a) *WOA*, (b) IAP, (c) EN4, and (d) HYCOM MR. Data are presented at seasonal resolution. Anomalies are computed by removing the climatological seasonal cycle of 1980–2010 and the linear trend of 1955–2010, and then smoothed with a five-season low-pass filter. The two black curves denote the 18° and 22°C isotherms. Solid gray contours highlight 0 values, and dashed gray contours are ±0.1, ±0.2, ±0.3, and ±0.4 K of temperature anomalies.

variations by HYCOM tend to penetrate to greater depths. This is likely related to a more diffuse thermocline in model, as indicated the fact that the 18°–22°C layer is thicker and deeper in HYCOM (black curves in Fig. 1). The variability characteristics described above, including the vertical structures, are observed in both the north and south IO basins separated by 10°S and well reproduced by HYCOM (Fig. S1).

One efficient way to characterize the primary vertical structures is by applying the empirical orthogonal function (EOF) algorithm. The vertically in-phase and out-of-phase anomalies immediately stand out as the two leading modes. These two types of variability together explain more than 90% of the total variance (Fig. 2). The vertically coherent variability, manifesting as the leading mode of the EOF, accounts for 70.5% of the total variance (dubbed ''mode 1'' hereafter). This type of variability shows the maximum amplitude typically at ~100 m and evident interdecadal variations (Fig. 2a). It showed a cooling tendency in 1960s, a warming in 1970s, a cooling from 1980 through 1997, and a subsequent warming from 1998 to 2015. The latter two were stronger and more prolonged than the formers. Besides these interdecadal changes, interannual fluctuations are also discernible with weaker amplitudes. The mode 1 in HYCOM MR possesses similar characters to the observed, but its maximum variability occurs at deeper depths (~150 m), again owing to the deeper thermocline in HYCOM. HYCOM well reproduced interdecadal changes since 1970s but underestimated the interannual component. As a result, its explained variance is lower (57.0%). The second mode (dubbed ''mode 2'' hereafter) shows a vertical dipole structure between the surface (0–60 m; T_1) and subsurface (60–400 m; T_2) layers and is dominated by interannual variations (Fig. 2b). HYCOM can realistically represent mode 2 in both vertical structure and time evolution, albeit with a higher explained percentage (27.8% vs 21.2%). Note that mode 1 and mode 2 only explain the detrended temperature variance, while the linear trend of 1995–2010 is rather strong and accounts for 54.9% of the original temperature variance.

EOF analysis is also performed for individual datasets (Fig. S2). *WOA*, IAP, and EN4 show nearly identical vertical structures to those in Fig. 2, with mode 1 and mode 2 explaining 75.3% and 18.5%, 69.4% and 22.2%, and 64.8% and 24.2%, respectively. Evident discrepancies are also seen among them in the time series of both modes, indicating considerable uncertainties. A comparison in power spectrum (Fig. 3) demonstrates that the interannual and interdecadal variances of mode 1 are both statistically significant, and

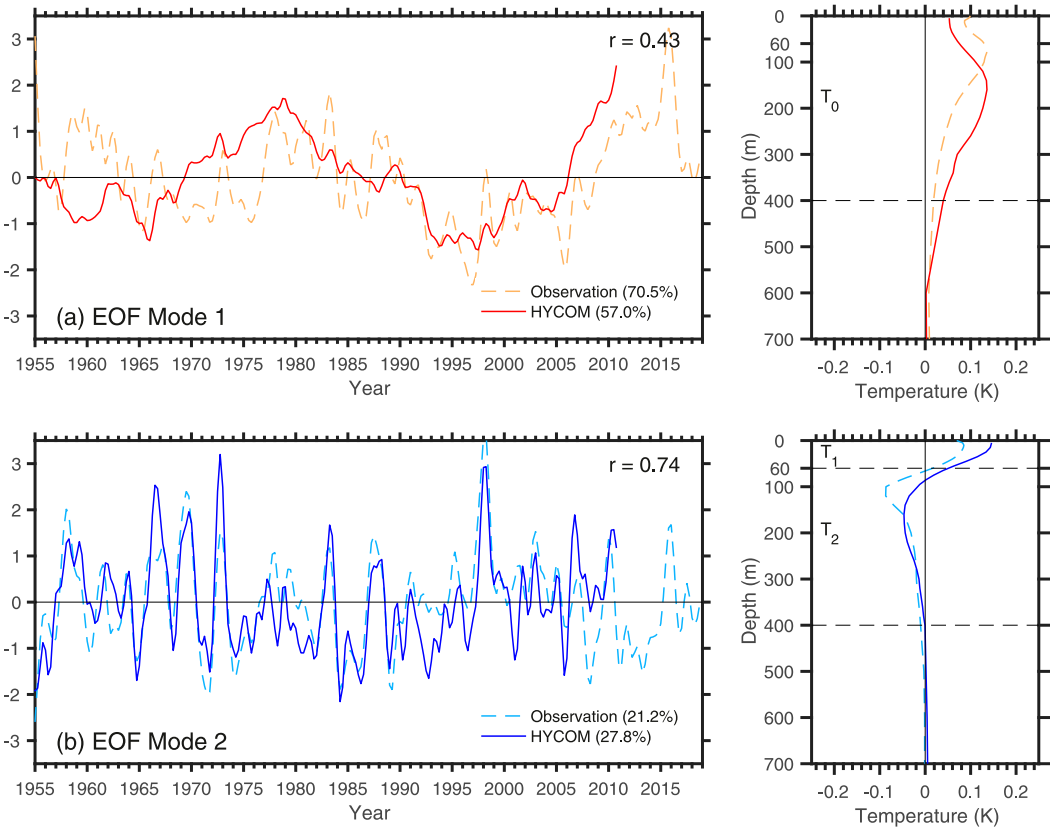

FIG. 2. The (a) first and (b) second EOF modes of the IO basin-mean temperature from ensemble-mean observation (dashed) and HYCOM MR (solid). (left) Time series and (right) vertical structure of the modes are shown.

HYCOM well captured the decadal-to-interdecadal variability with periods longer than 14 years but underestimated the variability on shorter time scales. For mode 2, the interannual spectral peaks exceed 90% confidence level in both observation and HYCOM. It seems that the two modes derived from HYCOM are better separated in frequency than in observation.

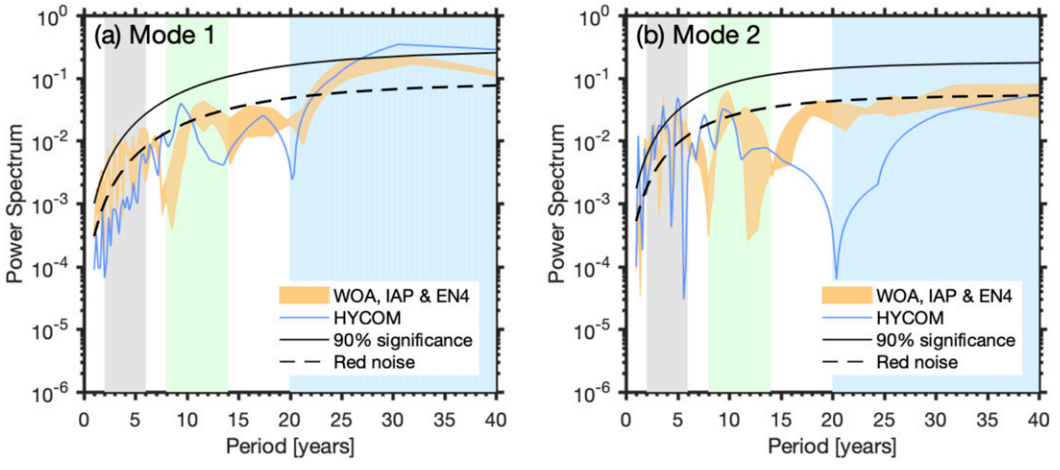

FIG. 3. Power spectra for the (a) first and (b) second EOF modes, derived from *WOA*, IAP, EN4, and HYCOM MR. The yellow shading denotes the spread of three observational datasets. The curves of 90% significance and red noise are computed with the ensemble-mean observational data. The gray, green, and blue shadings denote the interannual (2–6 years), decadal (8–14 years), and interdecadal (20–40 years) bands, respectively.

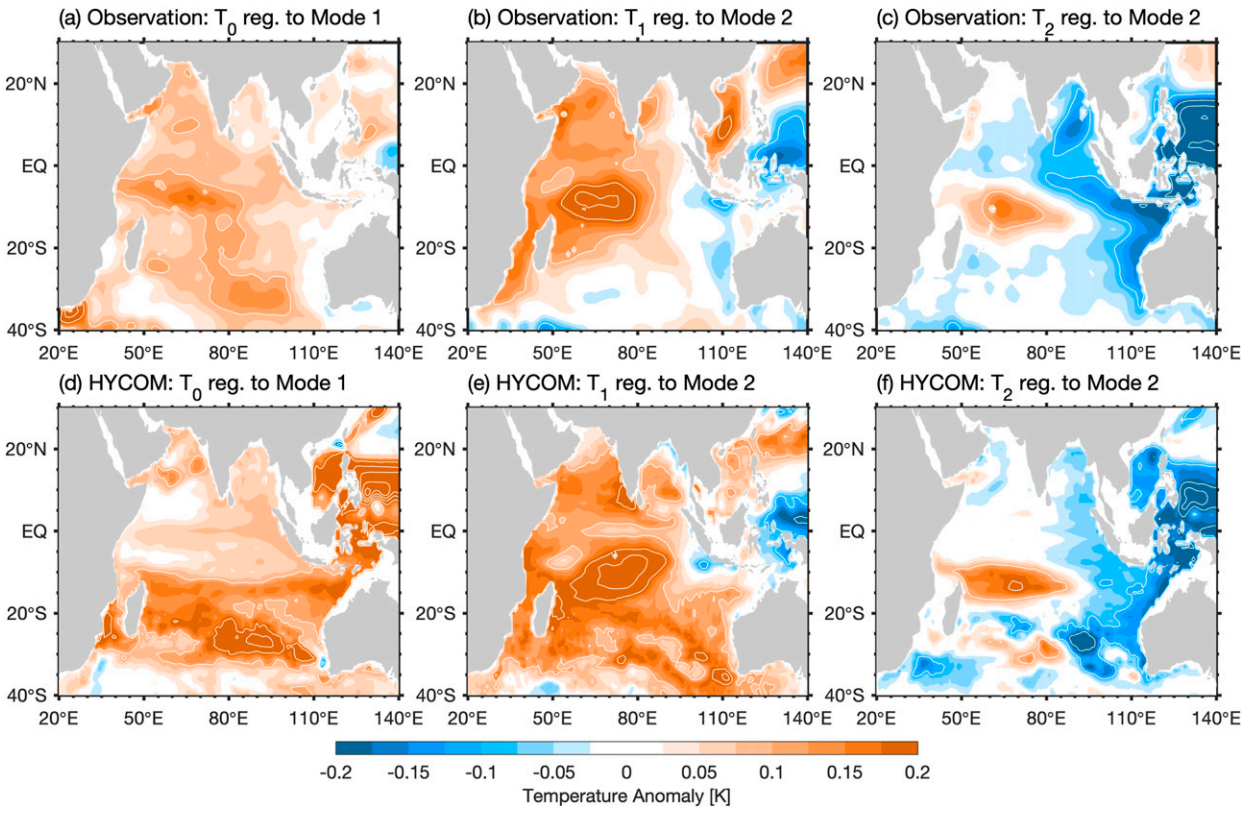

FIG. 4. Regression maps of layer-mean temperature onto EOF modes. (a) Upper-layer temperature (0–400-m average; T_0) regressed onto mode 1, (b) surface temperature (0–60-m average; T_1) regressed onto mode 2, and (c) subsurface temperature (60–400 m; T_2) regressed onto mode 2 derived from observation. (d)–(f) As in (a)–(c), but derived from HYCOM MR.

Horizontal distributions of these two types of variability are also of interest, which are achieved by regressing the 0–400-m average temperature (T_0) onto mode 1 and regressing the 0–60- and 60–400-m temperatures (T_1 and T_2) onto mode 2. The positive phase of mode 1 is characterized by basinwide warming over the IO with enhanced signatures (>0.1 K) in the south IO (Fig. 4a). In the positive phase of mode 2, the surface warming occurs mainly in the western-to-central IO basin and achieves the largest amplitude (>0.2 K) in the southwest tropical IO (Fig. 3b), while the subsurface cooling is seen mainly in the eastern IO basin (Fig. 4c). The spatial structures simulated by HYCOM (Figs. 4d–f) are overall consistent with those from observation. Detailed discrepancies are also discerned such as the stronger T_0 warming near the exit of the ITF in HYCOM (Fig. 4d). The two modes are tightly linked to important variables, such as OHC and SST. Mode 1 dominates the variability of total upper OHC (0–400) integrated over the IO, showing a linear correlation of $r = 0.86$ (Fig. S3a). A positive tendency of mode 1 represents heat uptake of the upper IO. Interdecadal variations of mode 1 are also associated with those of the IO basin-mean SST (Fig. S3b). The correlation of $r = 0.53$ is significant at 95% confidence level, although the effective degree of freedom is rather low due to low-pass filtering. Mode 2 is significantly correlated with interannual variability of the basin-mean SST, and the linear correlation reaches $r = 0.61$ (Fig. S3c). Mode 2 also indicates heat redistribution between the surface and subsurface layers, and its positive phase indicates releasing of subsurface heat to the surface.

Figure 5a compares mode 1 with the IPO index. When the IPO was in its negative phase during the periods of 1970–77 and 1998–2014, mode 1 showed positive tendencies, and the positive condition of IPO during 1980–96 cooccurred with a persistent cooling of mode 1. To better clarify this relationship, we further compute the 6-yr running trend of mode 1 (gray dashed line in Fig. 5a) that quantifies the tendency of mode 1 on decadal-to-interdecadal time scales (e.g., Kosaka and Xie 2016). Using running windows of 5–8 years do not affect the result dramatically. It achieves a significant correlation of $r = -0.50$ with the IPO. Their out-of-phase

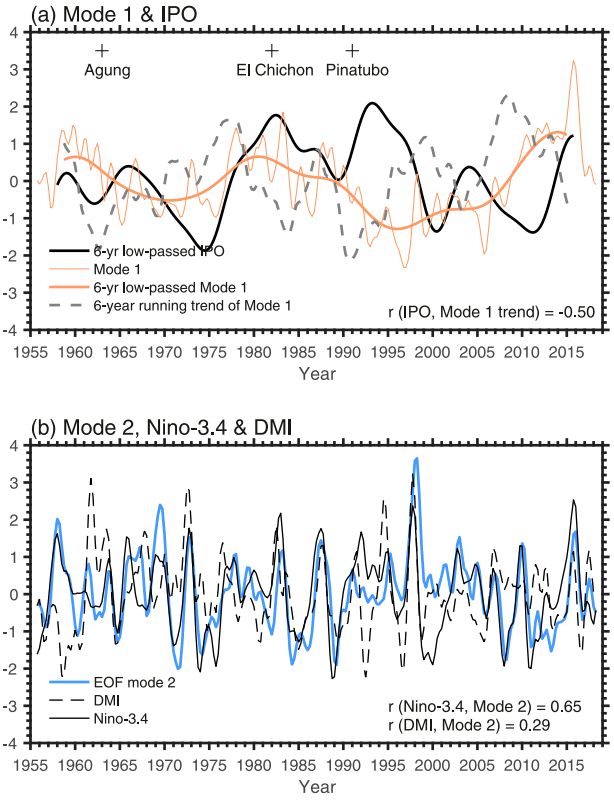

FIG. 5. Relationships between EOF modes and climate indices. (a) Normalized time series of mode 1, 6-yr low-passed mode 1, 6-yr low-passed IPO index, and the 6-yr running trend of mode 1. The plus signs mark the major volcano eruptions. (b) Normalized time series of EOF mode 2, DMI, and Niño-3.4. EOF modes are derived from ensemble-mean observational data, and all the climate mode indices are computed with HadISST data.

relationship is more obvious after the late 1970s, and in the 1960s the two showed likely in phase variations. Even after the late 1970s, the IPO cannot exclusively explain mode 1. Eruptions of major volcanos, such as the 1963 Agung, 1982 El Chichón, and 1991 Pinatubo, also evidently contributed to mode 1, as each of them cooccurred with rapid cooling of mode 1. As expected, mode 2 shows good relationships with ENSO and IOD, which are the two most influential interannual climate modes of the IO (Fig. 5b) with correlations of 0.65 and 0.29, respectively, with both exceeding 90% confidence. Either an El Niño or a positive IOD event is favorable for the positive phase of mode 2. Mode 1 and mode 2 are obtained by statistical analysis, representing two dominant types of variability with well-defined vertical structures. They are likely not intrinsic modes of the IO climate. Both IPO and radiation forcing (e.g., volcano eruptions) can give rise to mode 1, while ENSO and IOD mutually control mode 2. This is not surprising, given the strong impacts by the Pacific and external forcing on the IO climate (e.g., Klein et al. 1999; Cai et al. 2006, 2007; Du and Xie 2008; Han et al. 2014a, 2017). However, these two types of variability are important in ocean heat uptake and three-dimensional redistribution. Processes causing these two types of variability are worthy of in-depth investigation, which is the theme of the following section.

4. Generation mechanisms

a. The total variability

Figure 6 shows the simulated IO basin-mean temperature anomalies by HYCOM experiments. PAC represents the Pacific forcing effect through the ITF (Fig. 6a) and produces a large portion of decadal and interdecadal variations of the total variability in MR (Fig. 1d). Substantial variability occurs in the thermocline layer of 60–400 m, and the downward penetration tendency with time seen in MR is not obvious in PAC. These features are characteristic of baroclinic oceanic response to wind forcing. The baroclinic waves generated by Pacific winds enters the IO through the ITF and causes large variability in the thermocline. This process mainly contributes to decadal and interdecadal variabilities of mode 1. There are also interannual variations in surface temperature that are, however, much weaker than those in MR. The remnant variability in MR, as assessed by MR − PAC, is caused by local atmospheric forcing within the IO. The local forcing generates prominent temperature variations in both the surface and subsurface layers (Fig. 6b). The surface variability is stronger than that of PAC and close to that of MR in amplitude, suggesting the dominance of local atmospheric forcing in surface temperature variability, which is supported by the comparison of surface-layer OHC (OHC_1; 0–60 m) (Fig. 7a). The locally forced subsurface temperature anomalies are weaker in amplitude than those caused by the ITF, particularly for interdecadal, vertically coherent variations associated with mode 1. The subsurface OHC (OHC_2; 60–400 m) of PAC is of a larger standard deviation of 0.54×10^{22} J and a higher correlation ($r = 0.83$) with MR than that of MR − PAC (Fig. 7c).

The wind stress run (TAU) provides insights from another point of view. Variability in TAU (Fig. 6c) mostly resembles that of PAC but contains more interannual anomalies. The vertically out-of-phase anomalies are more evident in TAU than in PAC. Local wind forcing in the IO, which is the primary source for the difference between PAC and TAU, is one major process controlling mode 2. The difference between MR and TAU in temperature variability is primarily caused by

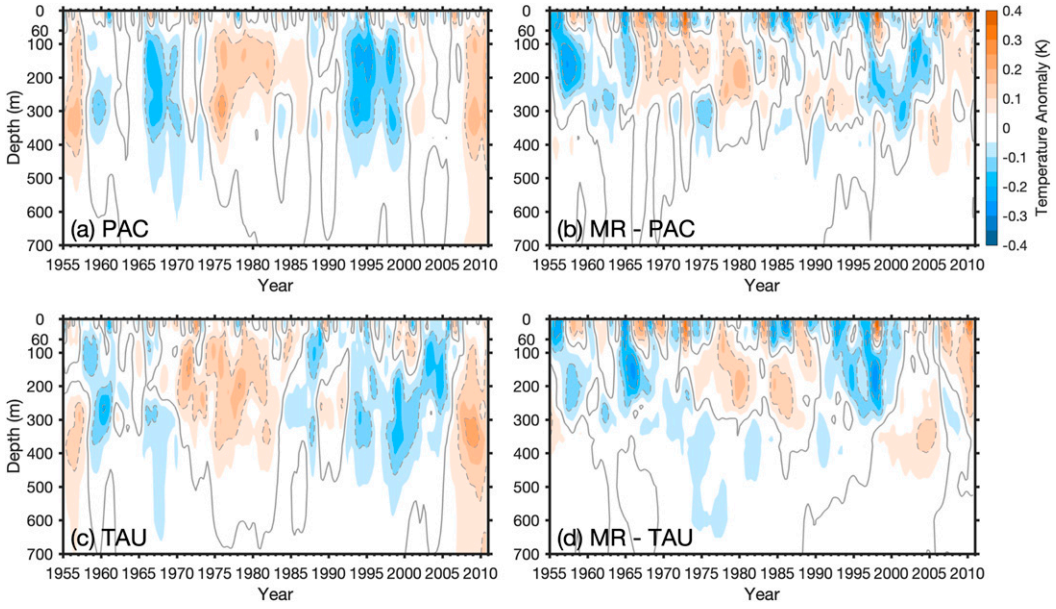

FIG. 6. IO basin-mean temperature anomaly from (a) PAC, (b) MR − PAC, (c) TAU, and (d) MR − TAU. Solid contours highlight zero values, and dashed contours are ±0.1, ±0.2, ±0.3, and ±0.4 K.

surface heat flux forcing (Fig. 6d), assuming a negligible role of freshwater flux. MR − TAU shows stronger surface variability and slightly weaker subsurface variability than TAU, as suggested by quantitative comparisons of OHC_1 and OHC_2 (Figs. 7c,d). Also noteworthy is that surface variations in Fig. 6d broadly resembles those in Fig. 6b (see also Figs. 7a and 7b). Local heat flux forcing in the IO is likely the primary cause for surface temperature variability. In comparison, the case of subsurface variability is more complex, with comparable contributions of different processes.

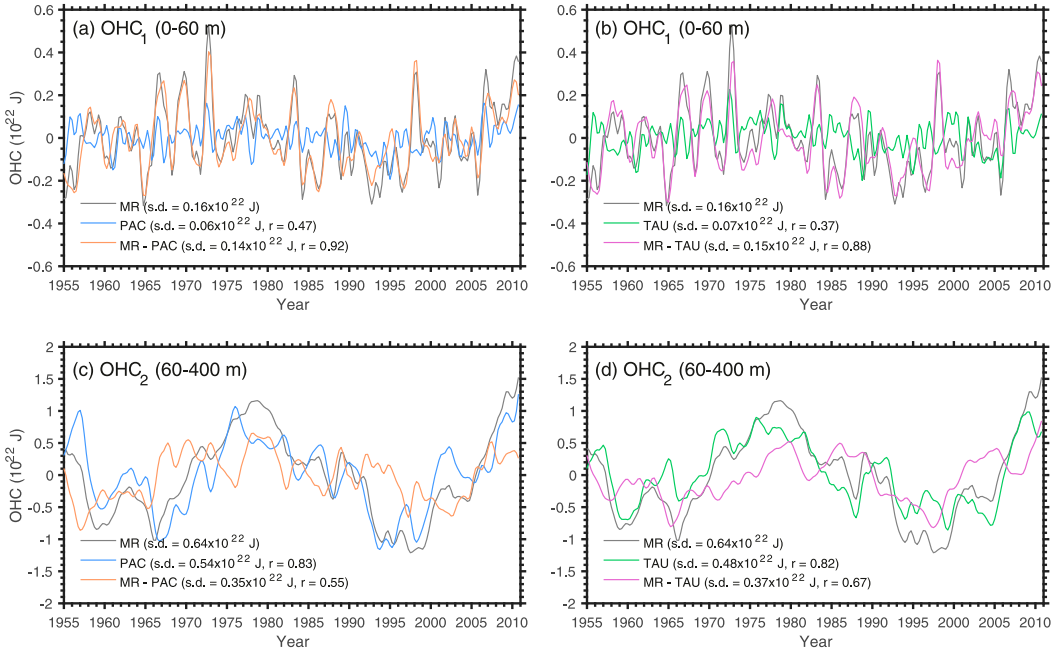

FIG. 7. (a) OHC_1 (0–60 m) and (c) OHC_2 (60–400 m) of the IO derived from MR, PAC, and MR − PAC. (b),(d) As in (a) and (c), but from MR, TAU, and MR − TAU.

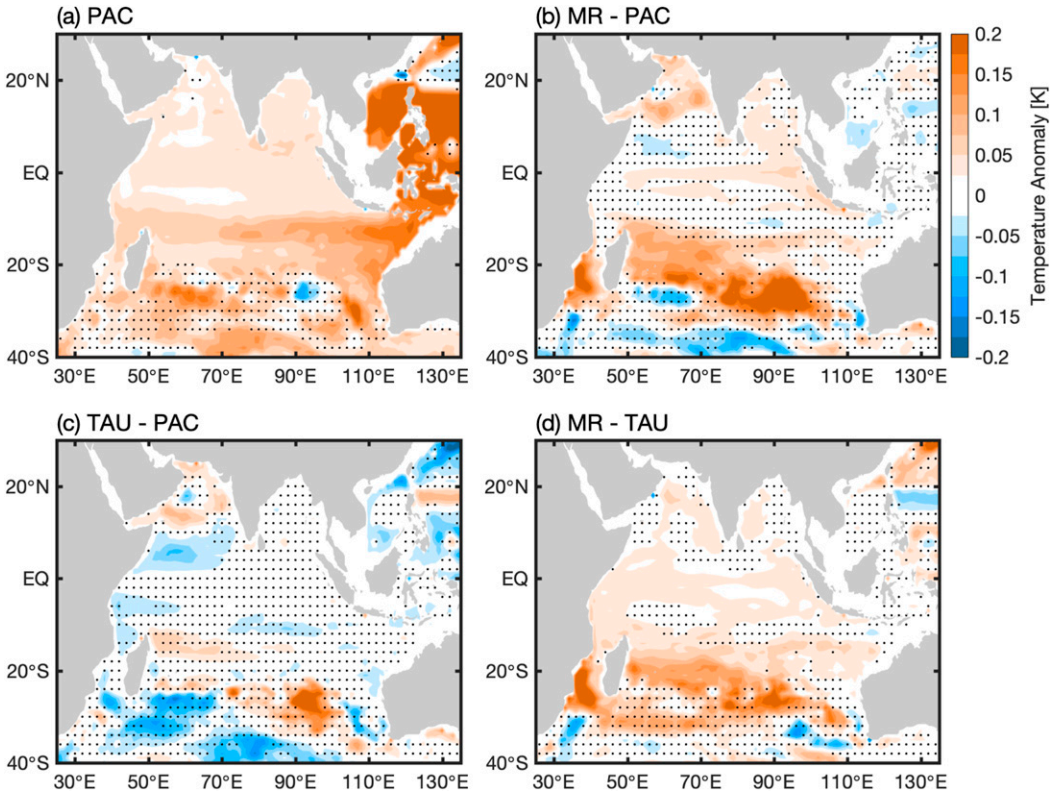

FIG. 8. Regression maps of T_0 (0–400-m average) of (a) PAC, (b) MR − PAC, (c) TAU − PAC, and (d) MR − TAU onto mode 1 of MR. Stippling indicates insignificant coefficients below 95% confidence level.

b. *Vertically coherent interdecadal variations*

Processes contributing to the vertically coherent interdecadal variability are explored in this subsection. Temperature anomalies of HYCOM experiments are regressed onto mode 1 of MR (Fig. 8). An enhanced ITF can cause a basinwide warming over the IO with stronger signatures in the southeast IO (Fig. 8a). The strong modulation effect of the ITF on the southern IO has been confirmed by many observational and modeling studies (e.g., Schwarzkopf and Böning 2011; Trenary and Han 2013; Ummenhofer et al. 2017; Jin et al. 2018), yet the influence on the northern IO was less discussed. The decadal warming signatures in the southern IO induced by the strengthened ITF can be communicated into the northern IO through meridional transport of ocean circulation (Li et al. 2018; Ma et al. 2019), especially via the western boundary currents (Schott et al. 2009). We need to state that this effect may be artificial or exaggerated in our Indo-Pacific simulation of HYCOM, because of the absence of the Agulhas leakage outflow to the Atlantic Ocean (e.g., Gordon 1985; Beal et al. 2011). Our model uses closed boundary conditions in the Agulhas leakage region and relaxes model temperature and salinity there to climatology. The effect of local atmospheric forcing is most influential in the central IO between 30° and 10°S (Fig. 8b), playing an essential role in the formation of the southern IO maximum in MR (Fig. 3d). Local forcing also contributes to the warmings of the equatorial and northern IO, and its effect on the Arabian Sea is stronger than that of the ITF. It can be further decomposed into the effects of local wind stress and surface heat fluxes. The former can be represented by TAU − PAC because the variability of ITF is mainly controlled by Pacific winds as indicated by the resemblance among MR, PAC, and TAU in ITF evolution (Li et al. 2018) (see also Fig. 9a). This effect is generally small except for the subtropical southern IO and the Arabian Sea (Fig. 8c). A large portion of warming signatures are caused by surface heat fluxes, as measured by MR − TAU, especially for the enhanced warming of the subtropical southern IO between 30° and 10°S (Fig. 8d). It is also discernible that the surface heat flux effect is weaker and less significant than the total anomaly in MR (Fig. 3d), which confirms the importance of ITF in mode 1. The summed effect of the ITF and surface heat fluxes are rather close to the total anomaly in MR.

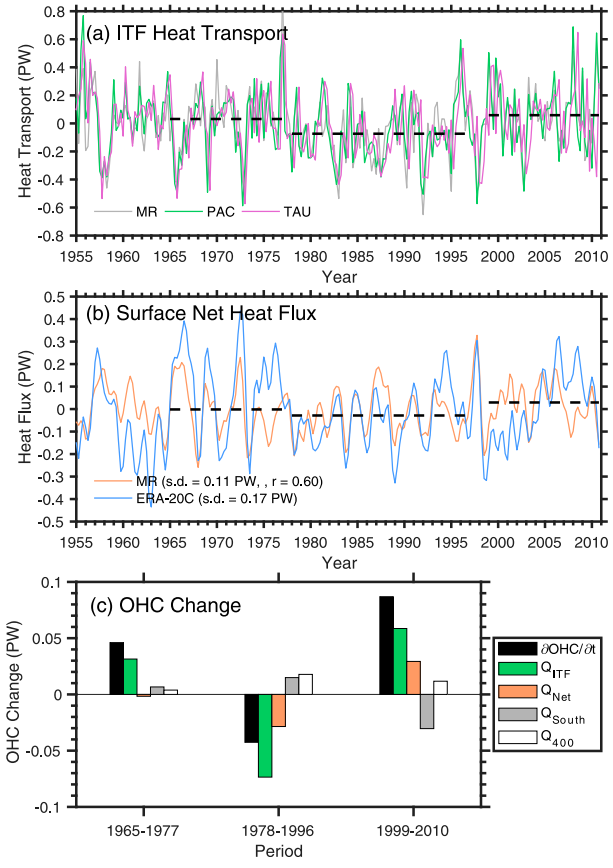

FIG. 9. (a) Heat transport anomalies of the ITF (1 PW = 10^{15} W) from MR, PAC, and TAU, computed as the integration of the meridional current and temperature over 106°–136°E and 0–400 m at 5°S with southward transport (toward the IO) defined as positive. (b) Surface net heat flux Q_{net} anomalies integrated over the IO basin from MR and ERA-20C. Average values of the 1965–77, 1978–96, and 1999–2010 periods are plotted as dashed straight lines. (c) The 0–400-m OHC tendency ($\partial OHC_0/\partial t$), ITF heat transport Q_{ITF}, IO-integrated Q_{net}, southern boundary heat transport Q_{South}, and IO-integrated vertical heat flux at 400-m Q_{400} for the three periods of 1965–77, 1978–96, and 1999–2010. Transport and flux toward the 0–400-m IO are defined as positive.

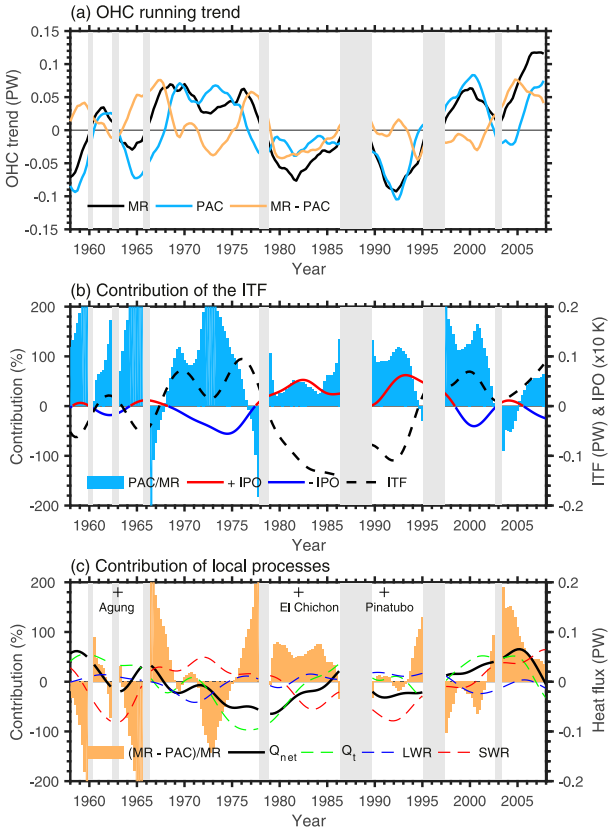

FIG. 10. (a) The 6-yr running trend of OHC_0 from MR, PAC, and MR − PAC. (b) Contribution of PAC to the 6-yr running trend of MR compared with the 6-yr low-pass-filtered ITF heat transport and IPO index. The correlation coefficient between MR OHC_0 running trend and IPO index is −0.71. (c) Contribution of MR − PAC to MR compared with the 6-yr low-pass-filtered Q_{net}, Q_T, LWR, and SWR. The gray shading denotes the periods with MR OHC_0 trend magnitude < 0.02 PW.

The essential roles played by the ITF and local heat flux forcing in causing the warming/cooling tendencies of the upper IO can be further examined through a simplified budget analysis,

$$\partial OHC_0/\partial t = Q_{ITF} + Q_{net} + Q_{South} + Q_{400} \qquad (2)$$

where OHC_0 is the 0–400-m heat content of the IO covarying with mode 1, Q_{ITF} is the heat transport of ITF, Q_{South} is the heat transport across the southern boundary of the IO, and Q_{net} and Q_{400} are vertical heat fluxes at sea surface and the lower boundary (400 m) integrated over the IO, respectively. Three periods are chosen: the warming periods of 1965–77 and 1999–2010 with continuous positive tendencies and the cooling period of 1978–96 with continuous negative tendencies (see also Fig. 10a). The two years of 1997–98 are greatly affected by an extreme El Niño and not considered here. Q_{ITF} showed large variations for all the three periods (Fig. 9a), while Q_{net} showed evident anomalies in the latter two periods (Fig. 9b). Figure 9c compares contributions of all terms to $\partial OHC_0/\partial t$ for the three periods. Q_{ITF} and Q_{net} were able to explain the majority of $\partial OHC_0/\partial t$, and the contribution of Q_{ITF} was larger. One may notice that during 1978–96, the negative $\partial OHC_0/\partial t$ is evidently smaller than the sum of Q_{ITF} and Q_{net}. This imbalance can be largely explained by Q_{South} and Q_{400} changes. There was a notable tendency of the increasing importance of Q_{net}. Its contribution was negligible in 1965–77 and became comparable to Q_{ITF} in the latter two periods.

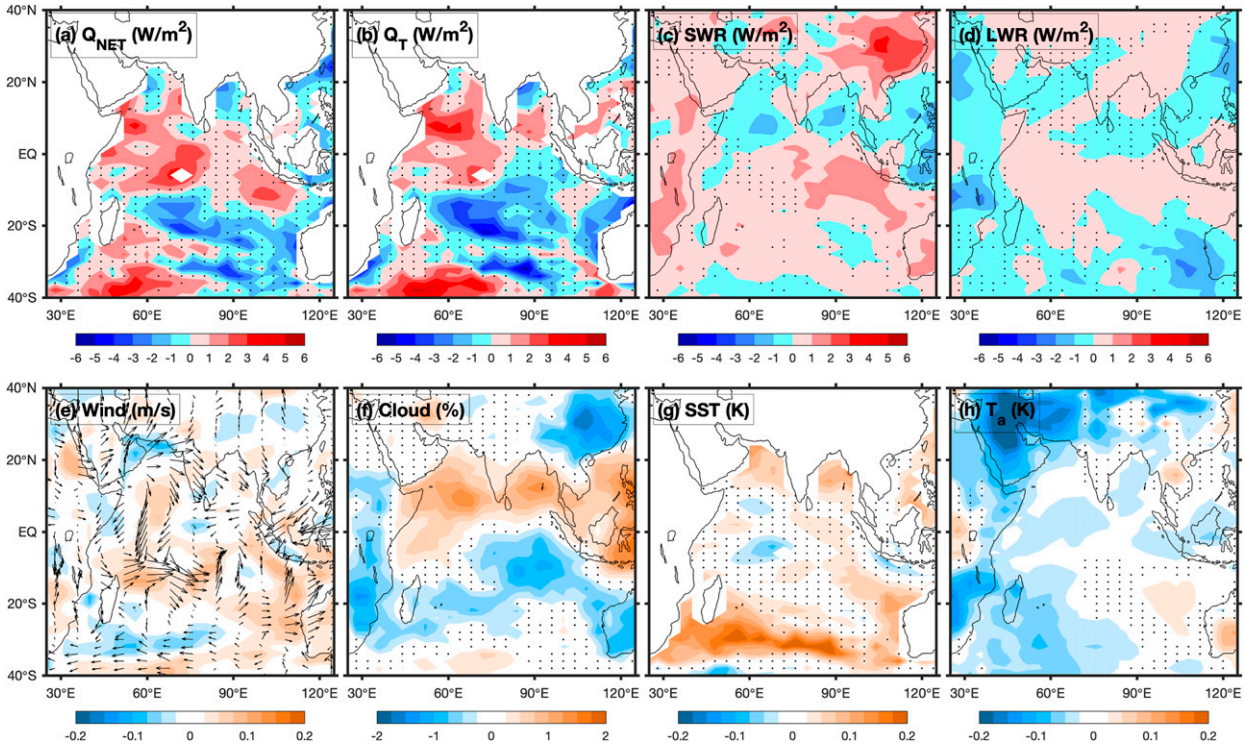

FIG. 11. Regressions of (a) surface net heat flux Q_{net}, (b) surface turbulent heat flux Q_T, (c) SWR, (d) LWR, (e) 10-m winds (vectors) and wind speed (color shading), (f) total could cover, (g) SST, and (h) 2-m air temperature T_a onto the 6-yr running trend of OHC_0. Q_{net}, Q_T, and SST are derived from HYCOM MR, while other variables are from ERA-20C data. Stippling indicates insignificant coefficients below 95% confidence level.

To better understand the time-varying mechanisms of mode 1, we plot in Fig. 10a the 6-yr running trend of OHC_0 derived from MR, PAC, and MR – PAC. Local atmospheric forcing (MR – PAC) played a major role in several short periods such as 1979–85 and 2003–07. We quantify the contribution of the ITF using the PAC-to-MR ratio of the OHC_0 trend, which shows evident temporal variations (Fig. 10b). Continuous domination of the ITF effect with contribution close to or exceeding +100% occurred over 1969–74, 1990–94, and 1998–2002. All of these periods were characterized by persistent anomalies of IPO and ITF. The ITF was strengthened during the negative IPO conditions of 1969–74 and 1998–2002 and weakened during the positive IPO condition of 1990–94. There were several periods worthy of further discussion. The ITF was also greatly weakened in the early 1980s, but its contribution was below 50%. Surface heat flux forcing was important in this period, as indicated by a persistent, large contribution of MR – PAC to the total OHC_0 trend and negative anomalies of Q_{net} (Fig. 10c). Surface turbulent heat flux Q_T and SWR are the two primary contributors to Q_{net}. The eruption of El Chichón in 1982 caused negative SWR and played an essential role in promoting the cooling of 1990s. Similarly, the 1991 Pinatubo induced large SWR anomalies that were partly offset by positive LWR anomalies. The dominance of Q_{net} in the warming of 2003–07 was also owing to the positive anomalies of SWR and Q_T. Prior to the late 1970s, the ITF can explain most of OHC_0 trends, and local forcing made negative contribution (damping) in some years.

The large effect of Q_{net} after the late-1970s warrants further investigation. We regress relevant fields onto the 6-yr running trend of OHC_0. The increased Q_{net} associated with the IO warming mainly occurs in the tropics and the southwest subtropical basin (Fig. 11a). Note that this pattern does not directly correspond to the warming pattern due to the redistribution by ocean circulation. Li and Han (2015) demonstrate that the warming anomalies generated in other areas converge in the central subtropical southern IO through climatological circulation. Through this effect, the increased Q_{net} in the tropical IO and southwest IO may cause the basinwide warming of the subtropical southern IO (Fig. 8d). These downward Q_{net} anomalies are mainly contributed by Q_T and SWR (Figs. 11b,c), and LWR effect is generally weak (Fig. 11d).

There is a convergence of zonal winds discernible in the subtropical southern IO (Fig. 11e), accompanied by reduced total cloud cover (Fig. 11f) and SST warming (Fig. 11g). These atmospheric and oceanic anomalies are likely coupled. The SST warming destabilizes the atmospheric boundary layer and dispels low stratiform cloud that is the dominant cloud type in this region (e.g., Tozuka and Oettli 2018; Zhang et al. 2018b; Li et al. 2019). The reduced cloud cover increases SWR reaching sea surface (Fig. 11c) and further promotes the existing SST warming. The westerly winds in the southwest subtropical IO also favor the growth of SST warming by reducing wind speed (Fig. 11e) and upward Q_T (Fig. 11b). The low cloud–SWR–SST feedback (Li and Philander 1996) and wind–Q_T–SST feedback (Xie and Philander 1994) increase the downward Q_{net} and contribute to the enhanced upper-ocean warming in the subtropical southern IO as shown in Fig. 10b. The regression of surface air temperature T_a shows cooling corresponds to downward Q_T anomalies (Fig. 11h). Significant T_a warming emerges only in the southeast IO, but Q_T shows negative anomalies there owing to the high SST and enhanced wind speed (Figs. 11e,g). These distributions rule out a significant contribution of T_a on the IO basin warming. The regressed SST anomalies from PAC and TAU also show warming signatures in the subtropical southern IO but much weaker than those in MR (Fig. S4). This confirms that the SST warming is mainly caused by increased downward Q_{net} through air–sea feedbacks described above rather than dynamically forced by local or Pacific winds.

The situation in the tropical IO is dramatically different. The prevailing westerly wind anomalies reduce total wind speed only in the central tropical south IO between 15° and 5°S and the southern Bay of Bengal where Q_T shows positive anomalies. In the rest of the tropics, the total wind speed is increased, but Q_T still shows positive anomalies, in part due to the SST cooling (Fig. 11g). In the tropical IO, the climatological SST is high (>28°C) and reaches the criterion for deep convection (e.g., Gadgil et al. 1984; Waliser et al. 1993). A small SST anomaly may cause large changes in air–sea fluxes (e.g., Roxy 2014; Y. Li et al. 2016). Figure S4c demonstrates that the SST cooling in the central tropical IO is mainly driven by local wind forcing. The SST cooling also causes increased surface SWR in the tropical south IO (Fig. 11c) by reducing the high cloud that dominates the low latitudes (Fig. 11f). By contrast, the SST warming in the Arabian Sea and Bay of Bengal acts to increase the high cloud cover and reduce surface SWR.

The regression fields described above demonstrate that the overall effect of tropical and subtropical air–sea interaction processes in the IO is to increase the downward surface Q_{net} and foster persistent upward tendencies of mode 1. Note that the complex interactions can be triggered by either the IPO phase shifts through atmospheric and oceanic teleconnections or external forcing such as volcanos and greenhouse gas concentration changes. Mode 1 is likely controlled by a mixed mechanism with a range of processes and interactions, although the Pacific forcing through the ITF generally plays the leading role. The short records of observational data and model simulation hinder a more accurate and unambiguous attribution at the present stage. The strong interdecadal fluctuations of mode 1 may exert significant feedback effects to both the Pacific and global climate, which is discussed in section 5.

c. *Vertical dipole-type interannual variability*

The positive phase of the vertical dipole-type variability (mode 2) manifests as surface warming in the western and central IO and subsurface cooling in the eastern IO (recall Fig. 3). Effects of different processes can be examined through regressing T_1 and T_2 onto mode 2 (Fig. 12). The basinwide warming of T_1 is primarily caused by local atmospheric forcing as measured by MR − PAC (Fig. 12b). TAU − PAC isolates the effect of local wind stress forcing, which causes a strong warming in the southwest tropical IO and prevailing cooling in the eastern tropical basin (Fig. 12c). These anomalies in surface temperature can be largely explained by oceanic wave response to the IO winds (e.g., Masumoto and Meyers 1998; Murtugudde et al. 2000; Xie et al. 2002; Huang and Kinter 2002; Rao and Behera 2005; Chen et al. 2016). Surface heat fluxes yield quasi-uniform warming over the IO (Fig. 12d) and largely offset the wind-driven cooling in the eastern tropical IO. Therefore, the basinwide surface warming of mode 2 is primarily caused surface heat fluxes, while wind forcing mainly acts to enhance the warming in the southwest tropical IO.

On the positive phase of mode 2, the ITF is responsible for the strong subsurface cooling in the southeast IO, with the maximal T_2 signatures near the coast of northwest Australia (Fig. 12e). This pattern mimics the Ningaloo Niña scenario (the negative phase of Ningaloo Niño), in which heat transport of the ITF is weakened due to relaxed Pacific trade winds in El Niño condition (e.g., Kataoka et al. 2014; Feng et al. 2013, 2015; Guo et al. 2020). The weaker cooling in equatorial and northern IO is mainly caused by local wind forcing (Figs. 12f,g). Therefore, the subsurface cooling of mode 2 is induced by winds local to the IO and Pacific winds, whereas the effect of surface heat fluxes is relatively weak for T_2 (Fig. 12h). These results are also helpful in understanding why the boundary of T_1 and T_2 occurs at

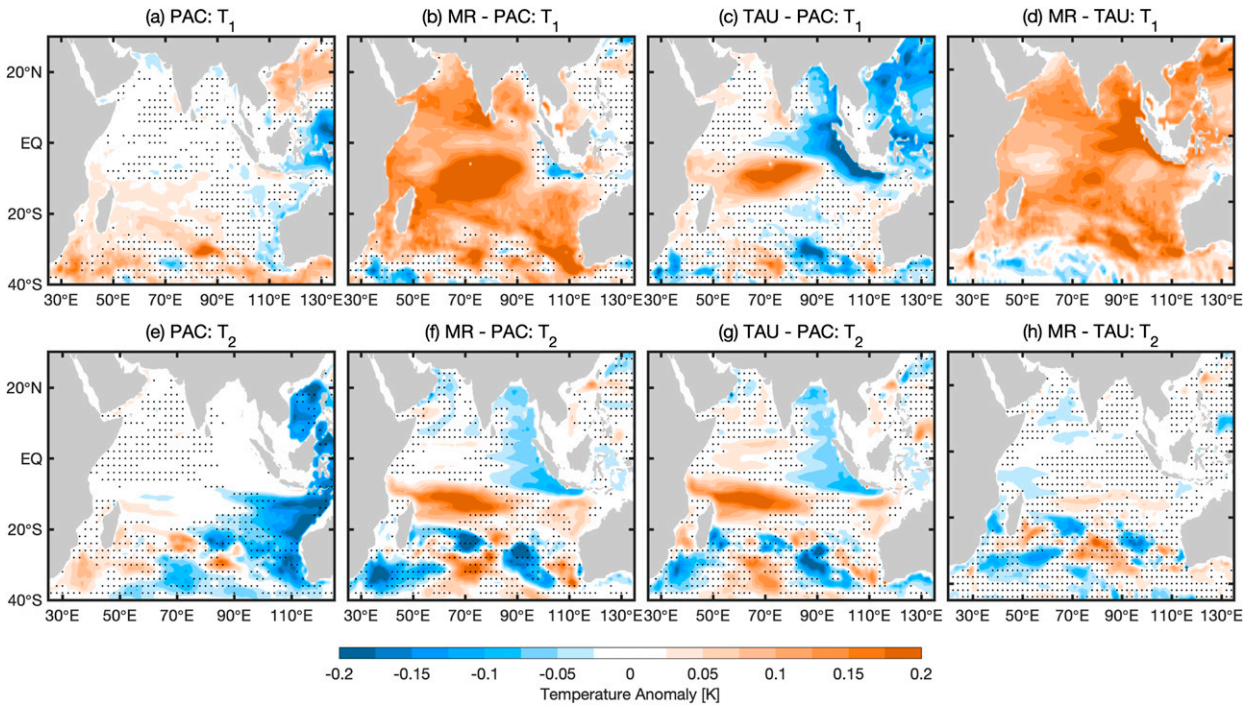

FIG. 12. Regression maps of T_1 (0–60-m average) of (a) PAC, (b) MR −PAC, (c) TAU − PAC, and (d) MR − TAU onto mode 2 of MR. (e)–(h) As in (a)–(d), but for regression maps of T_2 (60–400 m). Stippling indicates insignificant coefficients below 95% confidence level.

~60 m (Fig. 2b); 60 m roughly equals the mean depth of the mixed layer base in the IO (Keerthi et al. 2013). Temperature change of surface mixed layer is controlled by surface heat flux forcing, while temperature change below reflects the thermocline response to wind forcing.

ENSO and IOD are the two most influential climate regimes for the IO on interannual time scale. Their effects can be examined by the regressions of T_1 and T_2 onto representative indices (Fig. S5). The two exert similar effects on mode 2 over the tropical IO, except for stronger subsurface variations in the ENSO regression (Figs. S5b and S5e). One notable discrepancy between the two is the opposite signatures of T_1 and SST in the southeast IO. An El Niño favors surface cooling there, whereas a positive IOD causes surface warming (e.g., Zhang et al. 2018b). Regressions of relevant fields onto mode 2 aid us to understand the processes contributing to the surface warming (Fig. 13). The downward Q_{net} anomalies over the IO (Fig. 13a) contain major contributions from Q_T (Fig. 13b) determined largely by wind speed (Fig. 13e), SWR (Fig. 13c) controlled by cloud distribution (Fig. 13f), and SST (Fig. 13g). ENSO and IOD also have broadly similar signatures on surface heat fluxes, winds, and cloud distribution (Fig. S6). Considering the frequent cooccurrence of strong El Niño and positive IOD events, their effects may have been mixed in our regression fields, and it is, in fact, difficult to cleanly distinguish them. One discernible difference is that ENSO has stronger effects on the subtropical southern IO winds than the IOD (Figs. S6c,g), which may partly explain their discrepancies in T_2 (Figs. S5b,e).

It is instructive to further clarify why IPO causes vertically coherent anomalies in the IO (Fig. 5a), while ENSO induce vertical dipole anomalies (Fig. 5b), given that IPO largely represents decadal/interdecadal modulations of ENSO in tropics. Lead–lag regressions of temperature profiles onto Niño-3.4 and IPO indices provide insights into this issue (Fig. 14). It is shown that an El Niño causes a surface warming and a subsurface cooling during its mature and decaying stages (−3 to +12 months), while opposite anomalies emerge prior to its mature phase (−18 to −3 months) characterizing the transition from La Niña to El Niño conditions (Fig. 14a). The cooling is comparable in magnitude to the subsequent warming, with both primarily caused by surface heat flux forcing (Fig. 14b). These anomalies are superimposed on vertically coherent cooling tendencies generated by primarily by wind forcing (particularly the ITF; Fig. 14c) and also downward penetration of heat flux signatures. For our case, a positive IPO phase can be regarded as a period of >10 years with evidently stronger and more frequent El Niño events. Then surface warming and cooling anomalies tend to cancel each

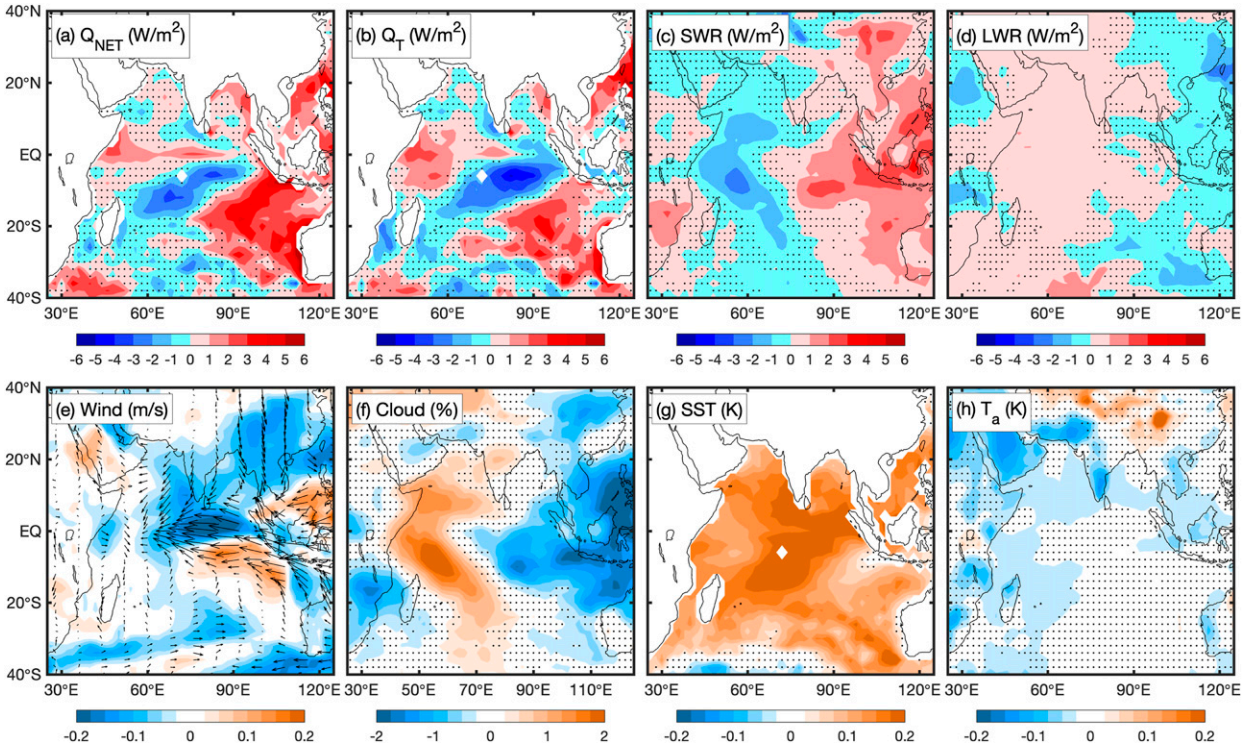

FIG. 13. Regressions of (a) surface net heat flux Q_{net}, (b) surface turbulent heat flux Q_T, (c) SWR, (d) LWR, (e) 10-m winds (vectors) and wind speed (color shading), (f) total could cover, (g) SST, and (h) 2-m air temperature T_a onto mode 2. Q_{net}, Q_T, and SST are derived from HYCOM MR, while other variables are from ERA-20C data. Stippling indicates insignificant coefficients below 95% confidence level.

other, whereas vertically coherent cooling tendencies integrate with time and give rise to a decadelong cooling, as indicated by the regression onto the 6-yr low-passed IPO index (Fig. 14b). Decadal air–sea feedback processes in the southern IO elucidated in section 4b also act to strengthen this vertically coherent cooling trend. The opposite scenario operates for a negative IPO period, in which the accumulation of warming tendencies by more

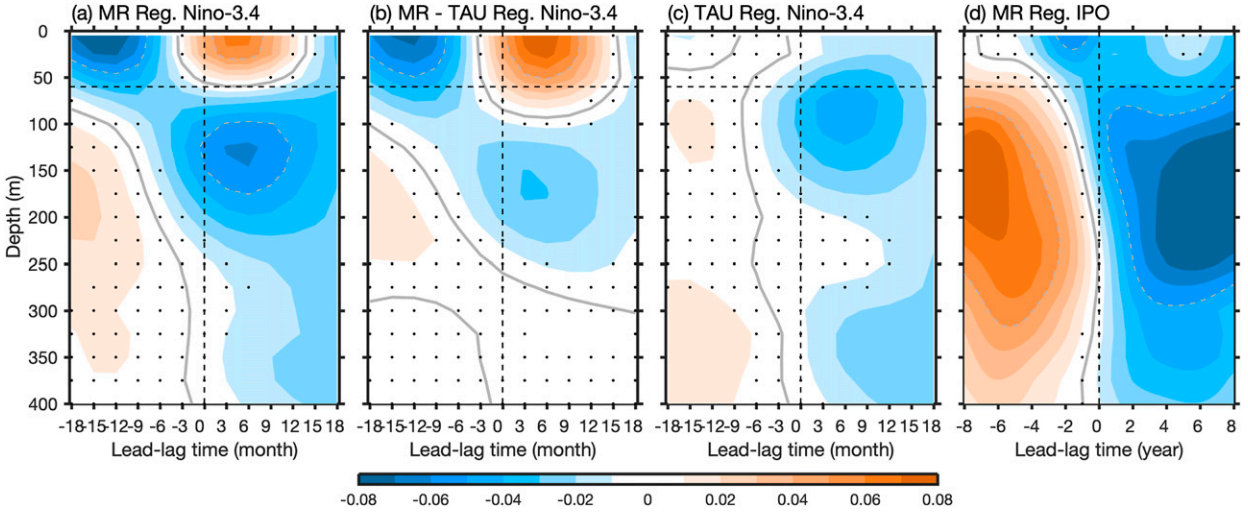

FIG. 14. Lead–lag regressions of IO basin-mean temperature anomalies from (a) MR, (b) MR − TAU, and (c) TAU onto the normalized Niño-3.4 index. Positive lead–lag time indicates leading by Niño-3.4. Solid contours highlight zero values, and dashed contours are ±0.05 K. Stippling indicates insignificant coefficients below 95% confidence level. (d) As in (a), but for the regression onto the 6-yr low-passed IPO index.

and stronger La Niña events leads to an overall warming trend in the IO.

5. Summary and discussion

The accumulated historical observations during the past half-century have documented prominent multi-time-scale thermal variabilities of the upper IO, leaving profound impacts on regional and global climate and posing challenges for scientific attribution and model prediction. This study resorts the observed upper-IO temperature variabilities from the perspective of vertical structure and identified two dominant types that explain the majority of interannual-to-interdecadal variance with the linear trend of 1955–2010 removed. The vertically coherent variability (mode 1) shows the maximal amplitude at ~100 m and evident interdecadal variations. Its positive phase is characterized by basinwide upper-ocean warming, with enhanced signatures in the central southern IO. The vertical dipole-type variability (mode 2) shows mainly interannual-to-decadal fluctuations. Its positive polarity shows prevailing surface warmings in the western and central IO and subsurface cooling in the eastern IO. Mode 1 can mostly represent variations of the upper-IO heat content and shows a lagged correlation with the IPO, whereas mode 2 is closely associated with ENSO, IOD, and interannual variability of the IO basin-mean SST. Indo-Pacific basin simulations of HYCOM are performed to explore the processes contributing to the two types of variability. Interdecadal variations of mode 1 are largely caused by Pacific wind forcing through the ITF and secondarily caused by surface heat fluxes within the IO. The relative importance of the two processes varies with time, and the contribution of heat fluxes has been comparable to the ITF during the 1978–96 cooling and 1999–2010 warming. The positive polarity of mode 2 involves a variety of processes associated with an El Niño or a positive IOD. The prevailing surface warming over the western and central IO is caused by the increased surface heat fluxes, while wind forcing mainly acts to enhance the southwest tropical IO warming through driving downwelling Rossby waves. Subsurface cooling anomalies in the equatorial eastern IO and the Bay of Bengal are induced by local wind forcing through upwelling Kelvin waves, whereas that in the southeast IO is mainly attributed to the weakened ITF.

In addition to a reorganization of existing knowledges under a new framework, there are also new findings achieved through analysis of the present study. They are remarked below.

1) In spite of indications for these two types of vertical structures in the huge body of existing literature, this study is the first attempt for quantification. It is revealed that the vertically coherent and dipole-type variabilities account for respectively 70.5% and 21.2% of the observed variance on interannual-to-interdecadal time scales, providing important insights into heat uptake and redistribution of the IO.
2) Interdecadal variations of the upper-IO temperature achieve the maximal amplitude in the subtropical southern IO. In addition to the forcing by ITF, this study suggests the importance of subtropical air–sea interactions in strengthening these interdecadal variations. The positive feedback of surface winds, Q_T, and SST, and that of low cloud, SWR, and SST work mutually to increase the total Q_{net} reaching sea surface over the subtropical southern IO.
3) This study put forward an explanation for different vertical structures of ENSO and IPO signatures on the IO temperature. An El Niño tends to cause a surface warming during its mature and decaying stages and a surface cooling prior to its development with comparable magnitudes, both through surface heat flux forcing (Fig. 14). When integrated over a positive IPO period of >10 years, these surface anomalies tend to offset each other, so that vertical dipole anomalies are largely damped. Meanwhile, vertically coherent cooling tendencies established by the weakened ITF accumulate constructively owing to stronger and more frequent El Niño events during a positive IPO phase, which gives rise to a decadelong cooling trend in the upper IO.

The two types of variability are of importance for the regional and global climate in many senses. A positive polarity of mode 2 releases heat from the thermocline to the air–sea interface, causing a short-term surge of the IO SST and exert strong modulation effects on synoptic atmospheric and oceanic perturbations as such tropical cyclones, marine heatwaves, and monsoon spells. One potential impact of mode 1 is on the interbasin SST gradient over the tropical Indo-Pacific basin that may affect the strength of the Pacific trade winds (Luo et al. 2012; Han et al. 2014b; Zhang and Karnauskas 2017). As demonstrated in section 4b, interdecadal variations of mode 1 are not purely responses to the IPO but contain external forcing effects such as greenhouse gases and volcanos that endow mode 1 with signals independent of the Pacific climate. The downward trends of mode 1 in the early 1990s are in part caused by the Pinatubo eruption and slashed the interbasin SST gradient ΔSST, while its upward trend during the 2000s raised ΔSST by causing a warming of the IO (Fig. S7a). ΔSST shows a

tight relationship with the strength of Pacific trade winds as quantified by the average 10-m zonal wind over the western and central tropical Pacific Ocean (Fig. S7b). Anomalies of ΔSST may have enhanced the decadal and interdecadal fluctuations of the Pacific trade winds, particularly for unprecedented intensification of Pacific trade winds during the 2000s. The strengthened Pacific trades reinforced the upward trend of mode 1 through the increased ITF heat transport. As such, a positive feedback loop is formed and acts to amplify the existing low-frequency climate anomalies over the Indo-Pacific basin. This positive feedback effect by the IO is supported by Zhang et al. (2019b) using "pacemaker" experiments of a coupled model, although examined on centennial time scale.

At present, it is still difficult for an unambiguous attribution of the interdecadal variations of mode 1, owing to the short records of observation. The data and simulations used for our analysis cover at most two cycles of mode 1 (1955–77 and 1978–2010). We found competing effects of a variety of processes, including the IPO-forced ITF variability and heat flux forcing of both natural and external origins. The ITF heat transport appears to be the leading driver (Figs. 8–11), but its effect may have been overestimated by our model simulation owing to a lack of Agulhas leakage to the Atlantic Ocean. There are many opportunities in the future to improve the approaches of the present study and achieves more accurate and insightful understanding of the two modes, such as using longer data records (geochemical proxies may serve as a good choice), more realistic model configurations (near-global simulation with higher resolution and better forcing fields), and intercomparison or large-ensemble approach of climate models (to unambiguously distinguish external forcing and internal variability). Investigation of such low-frequency, deep-reaching oceanic mode provides a pathway forward for improving the understanding and prediction of the IO's response and feedback to climate change.

The present study addresses the IO thermal variability using depth coordinates (z levels), although HYCOM adopts isopycnal coordinates in the subsurface ocean. An alternative view of analysis on isopycnal surfaces also provides useful insights for the IO thermal variability under climate change (e.g., Bindoff and McDougall 2000; Durack and Wijffels 2010; Li and Wang 2015; Tomczak 2019). Such analysis extracts the density-compensated potential temperature and salinity anomalies and better reflects property changes of subsurface water masses in response to the changing climate. In this study, we adopt a "linear" approach in the design of HYCOM experiments and assumes a negligible nonlinearity between two effects. For example, the difference between MR and PAC is used to measure the effect of local forcing within the IO. This assumption is questionable. One way to estimate the nonlinearity effect is performing a counterpart experiment of PAC that uses opposite surface forcing fields (climatological forcing in the Pacific and daily forcing over IO) to confirm our results. These issues can be addressed in the future.

Acknowledgments. Three anonymous reviewers provided insightful comments. This research is supported by the National Key R&D Program of China (Grant 2019YFA0606702), the Strategic Priority Research Program of Chinese Academy of Sciences (Grant XDB-42000000), and National Natural Science Foundation of China (NSFC) Grants 41776001 and 41806001. F. Wang is supported by the National Program on Global Change and Air-Sea Interaction (Grant GASI-IPOVAI-01-01). W. Han and L. Zhang are supported by NSF-AGS 1446480 and NSF-OCE 1658132. We thank NCAR CISL for the computational support in performing HYCOM simulations on the Yellowstone supercomputer. *WOA*, EN4, and IAP data are obtained from NOAA's NODC website https://www.nodc.noaa.gov/OC5/indprod.html, Met Office website https://www.metoffice.gov.uk/hadobs/en4/, and Lijing Cheng's website http://159.226.119.60/cheng/, respectively. HadISST data are available on the Met Office website https://www.metoffice.gov.uk/hadobs/hadisst/. ERA-20C data are downloaded from ECMWF interface website https://www.ecmwf.int/en/forecasts/datasets. Figures of this paper were produced with a licensed MATLAB 2018a program.

REFERENCES

Alory, G., S. Wijffels, and G. Meyers, 2007: Observed temperature trends in the Indian Ocean over 1960–1999 and associated mechanisms. *Geophys. Res. Lett.*, **34**, L02606, https://doi.org/10.1029/2006GL028044.

Annamalai, H., R. Murtugudde, J. Potemra, S. P. Xie, P. Liu, and B. Wang, 2003: Coupled dynamics over the Indian Ocean: Spring initiation of the zonal mode. *Deep-Sea Res. II*, **50**, 2305–2330, https://doi.org/10.1016/S0967-0645(03)00058-4.

——, P. Liu, and S.-P. Xie, 2005: Southwest Indian Ocean SST variability: Its local effect and remote influence on Asian monsoons. *J. Climate*, **18**, 4150–4167, https://doi.org/10.1175/JCLI3533.1.

——, K. Hamilton, and K. R. Sperber, 2007: The South Asian summer monsoon and its relationship with ENSO in the IPCC AR4 simulations. *J. Climate*, **20**, 1071–1092, https://doi.org/10.1175/JCLI4035.1.

Barnett, T. P., D. W. Pierce, K. M. AchutaRao, P. J. Gleckler, B. D. Santer, J. M. Gregory, and W. M. Washington, 2005: Penetration of human-induced warming into the world's oceans. *Science*, **309**, 284–287, https://doi.org/10.1126/science.1112418.

Beal, L. M., and Coauthors, 2011: On the role of the Agulhas system in ocean circulation and climate. *Nature*, **472**, 429–436, https://doi.org/10.1038/nature09983.

Behera, S. K., and T. Yamagata, 2001: Subtropical SST dipole events in the southern Indian Ocean. *Geophys. Res. Lett.*, **28**, 327–330, https://doi.org/10.1029/2000GL011451.

Bindoff, N. L., and T. J. McDougall, 2000: Decadal changes along an Indian ocean section at 32°S and their interpretation. *J. Phys. Oceanogr.*, **30**, 1207–1222, https://doi.org/10.1175/1520-0485(2000)030<1207:DCAAIO>2.0.CO;2.

Bleck, R., 2002: An oceanic general circulation model framed in hybrid isopycnic-Cartesian coordinates. *Ocean Modell.*, **4**, 55–88, https://doi.org/10.1016/S1463-5003(01)00012-9.

Cai, W., G. Meyers, and G. Shi, 2005: Transmission of ENSO signal to the Indian Ocean. *Geophys. Res. Lett.*, **32**, L05616, https://doi.org/10.1029/2004GL021736.

——, D. Bi, J. Church, T. Cowan, M. Dix, and L. Rotstayn, 2006: Pan-oceanic response to increasing anthropogenic aerosols: Impacts on the Southern Hemisphere oceanic circulation. *Geophys. Res. Lett.*, **33**, L21707, https://doi.org/10.1029/2006GL027513.

——, T. Cowan, M. Dix, L. Rotstayn, J. Ribbe, G. Shi, and S. Wijffels, 2007: Anthropogenic aerosol forcing and the structure of temperature trends in the southern Indian Ocean. *Geophys. Res. Lett.*, **34**, L14611, https://doi.org/10.1029/2007GL030380.

——, and Coauthors, 2019: Pantropical climate interactions. *Science*, **363**, 6430, https://doi.org/10.1126/science.aav4236.

Chambers, D., B. Tapley, and R. Stewart, 1999: Anomalous warming in the Indian Ocean coincident with El Niño. *J. Geophys. Res.*, **104**, 3035–3047, https://doi.org/10.1029/1998JC900085.

Chen, G., W. Han, Y. Li, and D. Wang, 2016: Interannual variability of equatorial eastern Indian Ocean upwelling: Local versus remote forcing. *J. Phys. Oceanogr.*, **46**, 789–807, https://doi.org/10.1175/JPO-D-15-0117.1.

Cheng, L., F. Zheng, and J. Zhu, 2015: Distinctive ocean interior changes during the recent warming slowdown. *Sci. Rep.*, **5**, 14346, https://doi.org/10.1038/srep14346.

——, and Coauthors, 2016: XBT Science: Assessment of instrumental biases and errors. *Bull. Amer. Meteor. Soc.*, **97**, 924–933, https://doi.org/10.1175/BAMS-D-15-00031.1.

——, K. Trenberth, J. Fasullo, T. Boyer, J. Abraham, and J. Zhu, 2017: Improved estimates of ocean heat content from 1960 to 2015. *Sci. Adv.*, **3**, e1601545, https://doi.org/10.1126/sciadv.1601545.

——, G. Wang, J. P. Abraham, and G. Huang, 2018: Decadal ocean heat redistribution since the late 1990s and its association with key climate modes. *Ciamte*, **6**, 91, https://doi.org/10.3390/cli6040091.

Clarke, A. J., and X. Liu, 1994: Interannual sea level in the northern and eastern Indian Ocean. *J. Phys. Oceanogr.*, **24**, 1224–1235, https://doi.org/10.1175/1520-0485(1994)024<1224:ISLITN>2.0.CO;2.

Dai, A., T. Qian, K. E. Trenberth, and J. D. Milliman, 2009: Changes in continental freshwater discharge from 1948 to 2004. *J. Climate*, **22**, 2773–2792, https://doi.org/10.1175/2008JCLI2592.1.

Deepa, J. S., C. Gnanaseelan, R. Kakatkar, A. Parekh, and J. S. Chowdary, 2018: The interannual sea level variability in the Indian Ocean as simulated by an ocean general circulation model. *Int. J. Climatol.*, **38**, 1132–1144, https://doi.org/10.1002/joc.5228.

——, ——, S. Mohapatra, J. S. Chowdary, A. Karmakar, R. Kakatkar, and A. Parekh, 2019: The tropical Indian Ocean decadal sea level response to the Pacific decadal oscillation forcing. *Climate Dyn.*, **52**, 5045–5058, https://doi.org/10.1007/s00382-018-4431-9.

Deser, C., and A. S. Phillips, 2006: Simulation of the 1976/77 climate transition over the North Pacific: Sensitivity to tropical forcing. *J. Climate*, **19**, 6170–6180, https://doi.org/10.1175/JCLI3963.1.

Dong, L., and T. Zhou, 2014: The Indian Ocean sea surface temperature warming simulated by CMIP5 models during the twentieth century: Competing forcing roles of GHGs and anthropogenic aerosols. *J. Climate*, **27**, 3348–3362, https://doi.org/10.1175/JCLI-D-13-00396.1.

——, and M. J. McPhaden, 2017: Why has the relationship between Indian and Pacific Ocean decadal variability changed in recent decades? *J. Climate*, **30**, 1971–1983, https://doi.org/10.1175/JCLI-D-16-0313.1.

——, T. Zhou, A. Dai, F. Song, B. Wu, and X. Chen, 2016: The footprint of the inter-decadal Pacific Oscillation in Indian Ocean sea surface temperatures. *Sci. Rep.*, **6**, 21251, https://doi.org/10.1038/srep21251.

Du, Y., and S. P. Xie, 2008: Role of atmospheric adjustments in the tropical Indian Ocean warming during the 20th century in climate models. *Geophys. Res. Lett.*, **35**, L08712, https://doi.org/10.1029/2008GL033631.

——, T. Qu, and G. Meyers, 2008: Interannual variability of sea surface temperature off Java and Sumatra in a global GCM. *J. Climate*, **21**, 2451–2465, https://doi.org/10.1175/2007JCLI1753.1.

——, S.-P. Xie, G. Huang, and K. Hu, 2009: Role of air–sea interaction in the long persistence of El Niño–induced North Indian Ocean warming. *J. Climate*, **22**, 2023–2038, https://doi.org/10.1175/2008JCLI2590.1.

Duan, J., Y. Li, L. Zhang, and F. Wang, 2020: Impacts of the Indian Ocean dipole on sea level and gyre circulation of the western tropical Pacific Ocean. *J. Climate*, **33**, 4207–4228, https://doi.org/10.1175/JCLI-D-19-0782.1.

Durack, P. J., and S. E. Wijffels, 2010: Fifty-year trends in global ocean salinities and their relationship to broad-scale warming. *J. Climate*, **23**, 4342–4362, https://doi.org/10.1175/2010JCLI3377.1.

England, M. H., and Coauthors, 2014: Recent intensification of wind-driven circulation in the Pacific and the ongoing warming hiatus. *Nat. Climate Change*, **4**, 222–227, https://doi.org/10.1038/nclimate2106.

Feng, M., Y. Li, and G. Meyers, 2004: Multidecadal variations of Fremantle sea level: Footprint of climate variability in the tropical Pacific. *Geophys. Res. Lett.*, **31**, L16302, https://doi.org/10.1029/2004GL019947.

——, M. J. McPhaden, and T. Lee, 2010: Decadal variability of the Pacific subtropical cells and their influence on the southeast Indian Ocean. *Geophys. Res. Lett.*, **37**, L09606, https://doi.org/10.1029/2010GL042796.

——, ——, S.-P. Xie, and J. Hafner, 2013: La Niña forces unprecedented Leeuwin Current warming in 2011. *Sci. Rep.*, **3**, 1277, https://doi.org/10.1038/srep01277.

——, H. H. Hendon, S.-P. Xie, A. G. Marshall, A. Schiller, Y. Kosaka, N. Caputi, and A. Pearce, 2015: Decadal increase in Ningaloo Niño since the late 1990s. *Geophys. Res. Lett.*, **42**, 104–112, https://doi.org/10.1002/2014gl062509.

Gadgil, S., N. Joshi, and P. Joseph, 1984: Ocean-atmosphere coupling over monsoon regions. *Nature*, **312**, 141–143, https://doi.org/10.1038/312141a0.

Gleckler, P., T. Wigley, B. Santer, J. Gregory, K. AchutaRao, and K. Taylor, 2006: Krakatoa's signature persists in the ocean. *Nature*, **439**, 675, https://doi.org/10.1038/439675a.

Good, S. A., M. J. Martin, and N. A. Rayner, 2013: EN4: Quality controlled ocean temperature and salinity profiles and monthly objective analyses with uncertainty estimates. *J. Geophys. Res. Oceans*, **118**, 6704–6716, https://doi.org/10.1002/2013JC009067.

Gordon, A. L., 1985: Indian-Atlantic transfer of thermocline water at the Agulhas Retroflection. *Science*, **227**, 1030–1033, https://doi.org/10.1126/science.227.4690.1030.

Guo, Y., Y. Li, F. Wang, Y. Wei, and Z. Rong, 2020: Processes controlling sea surface temperature variability of Ningaloo Niño. *J. Climate*, **33**, 4369–4389, https://doi.org/10.1175/JCLI-D-19-0698.1.

Han, W., and P. J. Webster, 2002: Forcing mechanisms of sea level interannual variability in the Bay of Bengal. *J. Phys. Oceanogr.*, **32**, 216–239, https://doi.org/10.1175/1520-0485(2002)032<0216:FMOSLI>2.0.CO;2.

——, G. A. Meehl, and A. Hu, 2006: Interpretation of tropical thermocline cooling in the Indian and Pacific Oceans during recent decades. *Geophys. Res. Lett.*, **33**, L23615, https://doi.org/10.1029/2006GL027982.

——, and Coauthors, 2010: Patterns of Indian Ocean sea-level change in a warming climate. *Nat. Geosci.*, **3**, 546–550, https://doi.org/10.1038/ngeo901.

——, J. Vialard, M. J. McPhaden, T. Lee, Y. Masumoto, M. Feng, and W. P. M. de Ruijter, 2014a: Indian Ocean decadal variability: A review. *Bull. Amer. Meteor. Soc.*, **95**, 1679–1703, https://doi.org/10.1175/BAMS-D-13-00028.1.

——, and Coauthors, 2014b: Intensification of decadal and multi-decadal sea level variability in the western tropical Pacific during recent decades. *Climate Dyn.*, **43**, 1357–1379, https://doi.org/10.1007/s00382-013-1951-1.

——, G. A. Meehl, A. Hu, J. Zheng, J. Kenigson, J. Vialard, B. Rajagopalan, and Yanto, 2017: Decadal variability of the Indian and Pacific Walker cells since the 1960s: Do they covary on decadal timescales? *J. Climate*, **30**, 8447–8468, https://doi.org/10.1175/JCLI-D-16-0783.1.

——, D. Stammer, G. Meehl, A. Hu, F. Sienz, and L. Zhang, 2018: Multi-decadal trend and decadal variability of the regional sea level over the Indian Ocean since the 1960s: Roles of climate modes and external forcing. *Climate*, **6**, 51, https://doi.org/10.3390/cli6020051.

Henley, B., J. Gergis, D. Karoly, S. Power, J. Kennedy, and C. Folland, 2015: A tripole index for the interdecadal Pacific oscillation. *Climate Dyn.*, **45**, 3077–3090, https://doi.org/10.1007/s00382-015-2525-1.

Huang, B., and J. L. Kinter III, 2002: Interannual variability in the tropical Indian Ocean. *J. Geophys. Res.*, **107**, 3199, https://doi.org/10.1029/2001JC001278.

——, and J. Shukla, 2007a: Mechanisms for the interannual variability in the tropical Indian Ocean. Part I: The role of remote forcing from the tropical Pacific. *J. Climate*, **20**, 2917–2936, https://doi.org/10.1175/JCLI4151.1.

——, and ——, 2007b: Mechanisms for the interannual variability in the tropical Indian Ocean. Part II: Regional processes. *J. Climate*, **20**, 2937–2960, https://doi.org/10.1175/JCLI4169.1.

Izumo, T., and Coauthors, 2010: Influence of the state of the Indian Ocean dipole on the following year's El Niño. *Nat. Geosci.*, **3**, 168–172, https://doi.org/10.1038/ngeo760.

Jin, X., Y. Kwon, C. C. Ummenhofer, H. Seo, F. U. Schwarzkopf, A. Biastoch, C. W. Böning, and J. S. Wright, 2018: Influences of Pacific climate variability on decadal subsurface ocean heat content variations in the Indian Ocean. *J. Climate*, **31**, 4157–4174, https://doi.org/10.1175/JCLI-D-17-0654.1.

Kataoka, T., T. Tozuka, S. Behera, and T. Yamagata, 2014: On the Ningaloo Niño/Niña. *Climate Dyn.*, **43**, 1463–1482, https://doi.org/10.1007/s00382-013-1961-z.

Keerthi, M., M. Lengaigne, J. Vialard, C. de Boyer Montégut, and P. Muraleedharan, 2013: Interannual variability of the tropical Indian Ocean mixed layer depth. *Climate Dyn.*, **40**, 743–759, https://doi.org/10.1007/s00382-012-1295-2.

Klein, S. A., B. J. Soden, and N. C. Lau, 1999: Remote sea surface temperature variations during ENSO: Evidence for a tropical atmospheric bridge. *J. Climate*, **12**, 917–932, https://doi.org/10.1175/1520-0442(1999)012<0917:RSSTVD>2.0.CO;2.

Kosaka, Y., and S.-P. Xie, 2016: The tropical Pacific as a key pacemaker of the variable rates of global warming. *Nat. Geosci.*, **9**, 669–673, https://doi.org/10.1038/ngeo2770.

Latif, D., D. Dommenget, M. Dima, and A. Grotzner, 1999: The role of Indian Ocean sea surface temperature in forcing east African rainfall anomalies during December–January 1997/98. *J. Climate*, **12**, 3497–3504, https://doi.org/10.1175/1520-0442(1999)012<3497:TROIOS>2.0.CO;2.

Lee, S.-K., W. Park, M. O. Baringer, A. L. Gordon, B. Huber, and Y. Liu, 2015: Pacific origin of the abrupt increase in Indian Ocean heat content during the warming hiatus. *Nat. Geosci.*, **8**, 445–449, https://doi.org/10.1038/ngeo2438.

Lee, T., and M. J. McPhaden, 2008: Decadal phase change in large-scale sea level and winds in the Indo-Pacific region at the end of the 20th century. *Geophys. Res. Lett.*, **35**, L01605, https://doi.org/10.1029/2007GL032419.

Levitus, S., J. I. Antonov, T. P. Boyer, R. A. Locarnini, H. E. Garcia, and A. V. Mishonov, 2009: Global ocean heat content 1955–2008 in light of recently revealed instrumentation problems. *Geophys. Res. Lett.*, **36**, L07608, https://doi.org/10.1029/2008GL037155.

Li, T. M., and S. G. H. Philander, 1996: On the annual cycle of the eastern equatorial Pacific. *J. Climate*, **9**, 2986–2998, https://doi.org/10.1175/1520-0442(1996)009<2986:OTACOT>2.0.CO;2.

Li, X., S.-P. Xie, S. T. Gille, and C. Yoo, 2016: Atlantic-induced pan-tropical climate change over the past three decades. *Nat. Climate Change*, **6**, 275–279, https://doi.org/10.1038/nclimate2840.

Li, Y., and W. Han, 2015: Decadal sea level variations in the Indian Ocean investigated with HYCOM: Roles of climate modes, ocean internal variability, and stochastic wind forcing. *J. Climate*, **28**, 9143–9165, https://doi.org/10.1175/JCLI-D-15-0252.1.

——, and F. Wang, 2015: Thermocline spiciness variations in the tropical Indian Ocean observed during 2003–2014. *Deep-Sea Res. I*, **97**, 52–66, https://doi.org/10.1016/j.dsr.2014.12.004.

——, W. Han, W. Wang, and M. Ravichandran, 2016: Intraseasonal variability of SST and precipitation in the Arabian Sea during the Indian summer monsoon: Impact of ocean mixed layer depth. *J. Climate*, **29**, 7889–7910, https://doi.org/10.1175/JCLI-D-16-0238.1.

——, ——, and L. Zhang, 2017: Enhanced decadal warming of the southeast Indian Ocean during the recent global surface warming slowdown. *Geophys. Res. Lett.*, **44**, 9876–9884, https://doi.org/10.1002/2017GL075050.

——, ——, A. Hu, G. Meehl, and F. Wang, 2018: Multidecadal changes of the upper Indian Ocean heat content during 1965–2016. *J. Climate*, **31**, 7863–7884, https://doi.org/10.1175/JCLI-D-18-0116.1.

——, ——, L. Zhang, and F. Wang, 2019: Decadal SST variability in the southeast Indian Ocean and its impact on regional climate. *J. Climate*, **32**, 6299–6318, https://doi.org/10.1175/JCLI-D-19-0180.1.

Liu, W., S.-P. Xie, and J. Lu, 2016: Tracking ocean heat uptake during the surface warming hiatus. *Nat. Commun.*, **7**, 10926, https://doi.org/10.1038/ncomms10926.

Luo, J.-J., W. Sasaki, and Y. Masumoto, 2012: Indian Ocean warming modulates Pacific climate change. *Proc. Natl.*

Acad. Sci. USA, **109**, 18 701–18 706, https://doi.org/10.1073/pnas.1210239109.

Ma, J., M. Feng, B. M. Sloyan, and J. Lan, 2019: Pacific influences on the meridional temperature transport of the Indian Ocean. *J. Climate*, **32**, 1047–1061, https://doi.org/10.1175/JCLI-D-18-0349.1.

Maloney, E. D., and A. H. Sobel, 2004: Surface fluxes and ocean coupling in the tropical intraseasonal oscillation. *J. Climate*, **17**, 4368–4386, https://doi.org/10.1175/JCLI-3212.1.

Masumoto, Y., and G. Meyers, 1998: Forced Rossby waves in the southern tropical Indian Ocean. *J. Geophys. Res.*, **103**, 27 589–27 602, https://doi.org/10.1029/98JC02546.

Mohapatra, S., C. Gnanaseelan, and J. S. Deepa, 2020: Multidecadal to decadal variability in the equatorial Indian Ocean subsurface temperature and the forcing mechanisms. *Climate Dyn.*, **54**, 3475–3487, https://doi.org/10.1007/s00382-020-05185-7.

Murtugudde, R., J. P. McCreary, and A. J. Busalacchi, 2000: Oceanic processes associated with anomalous events in the Indian Ocean with relevance to 1997–1998. *J. Geophys. Res.*, **105**, 3295–3306, https://doi.org/10.1029/1999JC900294.

Neetu, S., M. Lengaigne, E. M. Vincent, J. Vialard, G. Madec, G. Samson, M. R. R. Kumar, and F. Durand, 2012: Influence of upper-ocean stratification on tropical cyclone-induced surface cooling in the Bay of Bengal. *J. Geophys. Res.*, **117**, C12020, https://doi.org/10.1029/2012JC008433.

Nieves, V., J. K. Willis, and W. C. Patzert, 2015: Recent hiatus caused by decadal shift in Indo-Pacific heating. *Science*, **349**, 532–535, https://doi.org/10.1126/science.aaa4521.

Pearce, A. F., and M. Feng, 2013: The rise and fall of the ''marine heat wave'' off Western Australia during the summer of 2010/2011. *J. Mar. Syst.*, **111–112**, 139–156, https://doi.org/10.1016/j.jmarsys.2012.10.009.

Poli, P., and Coauthors, 2016: ERA-20C: An atmospheric reanalysis of the twentieth century. *J. Climate*, **29**, 4083–4097, https://doi.org/10.1175/JCLI-D-15-0556.1.

Potemra, J. T., and R. Lukas, 1999: Seasonal to interannual modes of sea level variability in the western Pacific and eastern Indian Oceans. *Geophys. Res. Lett.*, **26**, 365–368, https://doi.org/10.1029/1998GL900280.

Power, S., T. Casey, C. Folland, A. Colman, and V. Mehta, 1999: Inter-decadal modulation of the impact of ENSO on Australia. *Climate Dyn.*, **15**, 319–324, https://doi.org/10.1007/s003820050284.

Ramsay, H. A., M. B. Richman, and L. M. Leslie, 2017: The modulating influence of Indian Ocean sea surface temperatures on Australian region seasonal tropical cyclone counts. *J. Climate*, **30**, 4843–4856, https://doi.org/10.1175/JCLI-D-16-0631.1.

Rao, S. A., and S. K. Behera, 2005: Subsurface influence on SST in the tropical Indian Ocean: Structure and interannual variability. *Dyn. Atmos. Oceans*, **39**, 103–135, https://doi.org/10.1016/j.dynatmoce.2004.10.014.

——, ——, Y. Masumoto, and T. Yamagata, 2002: Interannual subsurface variability in the tropical Indian Ocean with a special emphasis on the Indian Ocean dipole. *Deep-Sea Res. II*, **49**, 1549–1572, https://doi.org/10.1016/S0967-0645(01)00158-8.

Rayner, N. A., D. E. Parker, E. B. Horton, C. K. Folland, L. V. Alexander, D. P. Rowell, E. C. Kent, and A. Kaplan, 2003: Global analyses of sea surface temperature, sea ice, and night marine air temperature since the late nineteenth century. *J. Geophys. Res.*, **108**, 4407, https://doi.org/10.1029/2002JD002670.

Roxy, M., 2014: Sensitivity of precipitation to sea surface temperature over the tropical summer monsoon region—And its quantification. *Climate Dyn.*, **43**, 1159–1169, https://doi.org/10.1007/s00382-013-1881-y.

Saji, N. H., B. N. Goswami, P. N. Vinayachandran, and T. Yamagata, 1999: A dipole mode in the tropical Indian Ocean. *Nature*, **401**, 360–363, https://doi.org/10.1038/43854.

Sayantani, O., and C. Gnanaseelan, 2015: Tropical Indian Ocean subsurface temperature variability and the forcing mechanisms. *Climate Dyn.*, **44**, 2447–2462, https://doi.org/10.1007/s00382-014-2379-y.

Schott, F. A., and J. P. McCreary Jr., 2001: The monsoon circulation of the Indian Ocean. *Prog. Oceanogr.*, **51**, 1–123, https://doi.org/10.1016/S0079-6611(01)00083-0.

——, S. P. Xie, and J. P. McCreary Jr., 2009: Indian Ocean circulation and climate variability. *Rev. Geophys.*, **47**, RG1002, https://doi.org/10.1029/2007RG000245.

Schwarzkopf, F. U., and C. W. Böning, 2011: Contribution of Pacific wind stress to multi-decadal variations in upper-ocean heat content and sea level in the tropical south Indian Ocean. *Geophys. Res. Lett.*, **38**, L12602, https://doi.org/10.1029/2011GL047651.

Sérazin, G., B. Meyssignac, T. Penduff, L. Terray, B. Barnier, and J. M. Molines, 2016: Quantifying uncertainties on regional sea level change induced by multidecadal intrinsic oceanic variability. *Geophys. Res. Lett.*, **43**, 8151–8159, https://doi.org/10.1002/2016GL069273.

Smith, D. M., and Coauthors, 2016: Role of volcanic and anthropogenic aerosols in the recent global surface warming slowdown. *Nat. Climate Change*, **6**, 936–940, https://doi.org/10.1038/nclimate3058.

Srinivasu, U., M. Ravichandran, W. Han, S. Sivareddy, H. Rahman, Y. Li, and S. Nayak, 2017: Causes for the reversal of north Indian Ocean decadal sea level trend in recent two decades. *Climate Dyn.*, **49**, 3887–3904, https://doi.org/10.1007/s00382-017-3551-y.

Takahashi, C., and M. Watanabe, 2016: Pacific trade winds accelerated by aerosol forcing over the past two decades. *Nat. Climate Change*, **6**, 768–772, https://doi.org/10.1038/nclimate2996.

Thompson, P. R., C. G. Piecuch, M. A. Merrifield, J. P. McCreary, and E. Firing, 2016: Forcing of recent decadal variability in the equatorial and north Indian Ocean. *J. Geophys. Res. Oceans*, **121**, 6762–6778, https://doi.org/10.1002/2016JC012132.

Tomczak, M., 2019: A statistic of water mass intrusions in the south Indian Ocean between 100°E and 110°E. *Ocean Dyn.*, **69**, 301–311, https://doi.org/10.1007/s10236-019-01251-9.

Tozuka, T., and P. Oettli, 2018: Asymmetric cloud-shortwave radiation-sea surface temperature feedback of Ningaloo Niño/Niña. *Geophys. Res. Lett.*, **45**, 9870–9879, https://doi.org/10.1029/2018GL079869.

Trenary, L. L., and W. Han, 2008: Causes of decadal subsurface cooling in the tropical Indian Ocean during 1961–2000. *Geophys. Res. Lett.*, **35**, L17602, https://doi.org/10.1029/2008GL034687.

——, and ——, 2012: Intraseasonal-to-interannual variability of south Indian Ocean sea level and thermocline: Remote versus local forcing. *J. Phys. Oceanogr.*, **42**, 602–627, https://doi.org/10.1175/JPO-D-11-084.1.

——, and ——, 2013: Local and remote forcing of decadal sea level and thermocline depth variability in the south Indian Ocean. *J. Geophys. Res. Oceans*, **118**, 381–398, https://doi.org/10.1029/2012jc008317.

Ummenhofer, C. C., A. Biastoch, and C. W. Boning, 2017: Multidecadal Indian Ocean variability linked to the Pacific and implications for preconditioning Indian Ocean dipole events. *J. Climate*, **30**, 1739–1751, https://doi.org/10.1175/JCLI-D-16-0200.1.

Waliser, D. E., N. E. Graham, and C. Gautier, 1993: Comparison of the highly reflective cloud and outgoing longwave radiation datasets for use in estimating tropical deep convection. *J. Climate*, **6**, 331–353, https://doi.org/10.1175/1520-0442(1993)006<0331:COTHRC>2.0.CO;2.

Wang, G., L. Cheng, J. Abraham, and C. Li, 2018: Consensuses and discrepancies of basin-scale ocean heat content changes in different ocean analyses. *Climate Dyn.*, **50**, 2471–2487, https://doi.org/10.1007/s00382-017-3751-5.

Webster, P. J., A. M. Moore, J. P. Loschnigg, and R. R. Leben, 1999: Coupled ocean–atmosphere dynamics in the Indian Ocean during 1997–98. *Nature*, **401**, 356–360, https://doi.org/10.1038/43848.

Wijffels, S., and G. Meyers, 2004: An intersection of oceanic waveguides: Variability in the Indonesian Throughflow region. *J. Phys. Oceanogr.*, **34**, 1232–1253, https://doi.org/10.1175/1520-0485(2004)034<1232:AIOOWV>2.0.CO;2.

Xie, S.-P., and S. G. H. Philander, 1994: A coupled ocean-atmosphere model of relevance to the ITCZ in the eastern Pacific. *Tellus*, **46A**, 340–350, https://doi.org/10.3402/tellusa.v46i4.15484.

——, H. Annamalai, F. A. Schott, and J. P. McCreary Jr., 2002: Structure and mechanisms of south Indian Ocean climate variability. *J. Climate*, **15**, 864–878, https://doi.org/10.1175/1520-0442(2002)015<0864:SAMOSI>2.0.CO;2.

——, K. Hu, J. Hafner, H. Tokinaga, Y. Du, G. Huang, and T. Sampe, 2009: Indian Ocean capacitor effect on Indo-western Pacific climate during the summer following El Niño. *J. Climate*, **22**, 730–747, https://doi.org/10.1175/2008JCLI2544.1.

Xue, J., C. Sun, J. Li, and J. Mao, 2018: South Atlantic forced multidecadal teleconnection to the midlatitude south Indian Ocean. *Geophys. Res. Lett.*, **45**, 8480–8489, https://doi.org/10.1029/2018GL078990.

Yang, G., L. Liu, X. Zhao, Y. Li, Y. Duan, B. Liu, K. Huang, and W. Yu, 2019: Impacts of different types of ENSO events on thermocline variability in the southern tropical Indian Ocean. *Geophys. Res. Lett.*, **46**, 6775–6785, https://doi.org/10.1029/2019GL082818.

Yuan, D., and Coauthors, 2011: Forcing of the Indian Ocean dipole on the interannual variations of the tropical Pacific Ocean: Roles of the Indonesian Throughflow. *J. Climate*, **24**, 3593–3608, https://doi.org/10.1175/2011JCLI3649.1.

Zhang, L., and K. B. Karnauskas, 2017: The role of tropical interbasin SST gradients in forcing walker circulation trends. *J. Climate*, **30**, 499–508, https://doi.org/10.1175/JCLI-D-16-0349.1.

——, W. Han, and F. Sienz, 2018a: Unraveling causes for the changing behavior of the tropical Indian Ocean in the past few decades. *J. Climate*, **31**, 2377–2388, https://doi.org/10.1175/JCLI-D-17-0445.1.

——, ——, Y. L. Li, and T. Shinoda, 2018b: Mechanisms for generation and development of the Ningaloo Niño. *J. Climate*, **31**, 9239–9259, https://doi.org/10.1175/JCLI-D-18-0175.1.

——, ——, ——, and N. Lovenduski, 2019a: Variability of sea level and upper-ocean heat content in the Indian Ocean: Effects of subtropical Indian Ocean dipole and ENSO. *J. Climate*, **32**, 7227–7245, https://doi.org/10.1175/JCLI-D-19-0167.1.

——, ——, K. B. Karnauskas, G. A. Meehl, A. Hu, N. Rosenbloom, and T. Shinoda, 2019b: Indian Ocean warming trend reduces Pacific warming response to anthropogenic greenhouse gases: An interbasin thermostat mechanism. *Geophys. Res. Lett.*, **46**, 10 882–10 890, https://doi.org/10.1029/2019GL084088.

Zhou, X. B., O. Alves, S. J. Marsland, D. H. Bi, and A. C. Hirst, 2017: Multi-decadal variations of the south Indian Ocean subsurface temperature influenced by Pacific decadal oscillation. *Tellus*, **69A**, 1308055, https://doi.org/10.1080/16000870.2017.1308055.